

1 **Human iPSC modeling elucidates mutation-specific responses to gene therapy in a genotypically**
2 **diverse dominant maculopathy**

3

4 Divya Sinha^{1,2*}, Benjamin Steyer^{1,3*}, Pawan K. Shahi^{1,4}, Katherine Mueller³, Rasa Valiauga², Kimberly
5 L. Edwards², Cole Bacig², Stephanie S. Steltzer³, Sandhya Srinivasan³, Amr Abdeen³, Evan Cory³,
6 Viswesh Periyasamy³, Alireza Fotuhi Siahpirani³, Sushmita Roy^{3,5}, Bikash R. Pattnaik^{1,4,6**}, Krishanu
7 Saha^{1,3,7**}, David M. Gamm^{1,2,6**^}

8 ¹McPherson Eye Research Institute, University of Wisconsin-Madison, Madison, WI, USA

9 ²Waisman Center, University of Wisconsin-Madison, Madison, WI, USA

10 ³Wisconsin Institute for Discovery, University of Wisconsin-Madison, Madison, WI, USA

11 ⁴Department of Pediatrics, University of Wisconsin-Madison, Madison, WI, USA

12 ⁵Department of Biostatistics, University of Wisconsin-Madison, Madison, WI, USA

13 ⁶ Department of Ophthalmology and Visual Sciences, University of Wisconsin-Madison, Madison, WI,
14 USA

15 ⁷Department of Biomedical Engineering, University of Wisconsin-Madison, Madison, WI, USA

16 * These authors contributed equally to the work

17 ****Co-Correspondence:** D.M.G. (dgamm@wisc.edu), K.S. (ksaha@wisc.edu), and B. R. P.

18 (pattnaik@wisc.edu)

19 ^ **Lead contact:** D.M.G.

20 **Subject Terms:** human pluripotent stem cells, gene therapy, somatic cell genome editing CRISPR-Cas9,
21 gene augmentation, autosomal dominant disease, macular degeneration, orphan disease, channelopathy

22

23

24 SUMMARY

25 **Dominantly inherited disorders are not typically considered therapeutic candidates for gene**
26 **augmentation (GA). We tested whether GA or genome editing (GE) could serve as a solo therapy**
27 **for autosomal dominant Best disease (adBD), a macular dystrophy linked to over 100 mutations in**
28 **the *BEST1* gene, which encodes a homo-pentameric calcium-activated chloride channel (CaCC) in**
29 **the retinal pigment epithelium (RPE). Since no suitable animal models of adBD exist, we generated**
30 **RPE from patient-derived induced pluripotent stem cells (iPSC-RPE) and found that GA restored**
31 **CaCC activity and improved rhodopsin degradation in a subset of adBD lines. iPSC-RPE**
32 **harboring adBD mutations in calcium clasp or chloride binding domains of the channel, but not in**
33 **a putative structural region, were responsive to GA. However, reversal of the iPSC-RPE CaCC**
34 **deficit was demonstrated in every adBD line following targeted CRISPR-Cas9 GE of the mutant**
35 **allele. Importantly, 95% of GE events resulted in premature stop codons within the mutant allele,**
36 **and single cell profiling demonstrated no adverse perturbation of RPE transcriptional programs**
37 **post-editing. These results show that GA is a viable approach for a subset of adBD patients**
38 **depending on the functional role of the mutated residue. Further, GA non-responders are**
39 **candidates for targeted GE of the mutant allele. Similar scenarios likely exist for other**
40 **genotypically diverse dominant diseases, expanding the therapeutic landscape for affected patients.**

41 42 INTRODUCTION

43 Genotypically heterogeneous dominant diseases pose significant challenges and opportunities for
44 precision medicine (Doudna and Charpentier, 2014). Among gene therapies, GA for recessive disorders is
45 the most developed, having spurred multiple clinical trials (Cukras et al., 2018; Lam et al., 2019; Russell
46 et al., 2017) and FDA approval for one ocular disease (Ledford, 2017). However, GA is generally ruled
47 out as a stand-alone therapy for dominant disorders due to a perceived need to eliminate the deleterious

48 effects of the mutant (MT) allele. While GE holds promise in this regard (Bakondi et al., 2016; Li, 2018;
49 Tsai et al., 2018), testing safety and efficacy for every GE target mutation using MT allele-targeted single
50 guide RNAs (sgRNAs) presents practical and economic barriers. Further, GE cannot correct all mutations
51 (Bakondi et al., 2016; Courtney et al., 2016; Pattanayak et al., 2013) and may lead to off-target
52 mutagenesis—particularly within the heterozygous wildtype (WT) allele in dominant diseases—or other
53 adverse events (Cromer et al., 2018). As such, it is prudent to maximize use of GA in cases where it is
54 deemed safe and efficacious and reserve GE strategies for those patients who truly require it.

55 Best disease, a common type of inherited macular degeneration, is a genotypically complex
56 disorder transmitted predominantly as adBD, although rare cases of autosomal recessive bestrophinopathy
57 (ARB) are known (Johnson et al., 2017). Both adBD and ARB are caused by missense mutations in the
58 *BEST1* gene, which is expressed in the RPE, a monolayer of cells essential for the survival and function
59 of photoreceptors. While canine models of ARB closely mimic the human phenotype (Guziewicz et al.,
60 2017), no animal models of adBD exist. To provide a therapeutic testing platform for adBD, we
61 previously developed the first human iPSC-RPE models of the disease, which demonstrated relevant
62 cellular dysfunction; most notably, delayed degradation of phagocytosed photoreceptor outer segment
63 (POS) proteins (Singh et al., 2015; Singh et al., 2013b). Recently, the high-resolution crystal structure of
64 WT BEST1 was elucidated, which revealed it to be a homo-pentameric CaCC (Dickson et al., 2014; Yang
65 et al., 2014) (**Figure 1A**). Mutation hotspots in BEST1 were found to lie within calcium or chloride ion
66 binding sites, or contribute to the structural organization of the channel, among other roles (Dickson et al.,
67 2014). Our two prior adBD iPSC-RPE models harbored mutations in a calcium binding (N296H) or
68 structural (A146K) domain (Singh et al., 2015; Singh et al., 2013b). Therefore, for the present study, we
69 generated iPSCs from a third patient with adBD caused by a chloride binding site mutation (R218C), as
70 well as an ARB patient with compound heterozygous mutations (R141H/A195V) (**Figure 1B,C**). We also

71 employed two control lines: a WT iPSC line and an isogenic line generated via CRISPR-based gene
72 correction of R218C adBD iPSCs (Steyer et al., 2018).

73

74 **RESULTS**

75 **BEST1 protein is robustly expressed in WT and adBD iPSC-RPE, but not ARB iPSC-RPE.**

76 The six iPSC lines were tested for pluripotency, differentiated to RPE, and characterized (**Data**
77 **S1; Figure S1; Table S1**). iPSC-RPE monolayers from all adBD and control lines, but not the ARB line,
78 showed robust expression of BEST1 protein (**Figure S1D**). The profoundly decreased BEST1 expression
79 in our ARB cultures is consistent with reports using heterologous expression systems that showed low or
80 undetectable levels of R141H or A195V BEST1 (Milenkovic et al., 2018).

81

82 **Virus-mediated *BEST1* GA restores CaCC activity and enhances POS degradation in ARB iPSC-** 83 **RPE.**

84 We next sought to confirm that ectopic expression of wildtype human BEST1 (hBEST1) could
85 ameliorate the disease phenotype of R141H/A195V ARB iPSC-RPE, analogous to GA studies using ARB
86 canines or other iPSC-RPE model systems for ARB (Guziewicz et al., 2018; Li et al., 2017). For readouts
87 of efficacy, we performed single-cell patch clamp recordings of calcium-activated chloride current
88 density—a measurement of CaCC activity—which was greatly reduced in ARB iPSC-RPE cells relative
89 to WT iPSC-RPE (**Figure 1D; Figure S2**). As an assay of intact RPE monolayer function, we also
90 monitored degradation of rhodopsin following POS feeding (**Figure 2**).

91 For GA we used a lentivirus (LV) construct (*hVMD2-hBEST1-T2A-GFP*) (**Figure 2A**) designed to
92 co-express hBEST1 and GFP under control of the human *BEST1* promoter (*hVMD2*) in order to restrict
93 hBEST1 expression to RPE. Although adeno-associated virus (AAV) is commonly employed for gene

94 delivery *in vivo*, LV has also been used in human retinal gene therapy trials (Waugh et al., 2018)
95 (ClinicalTrials.gov Identifiers: NCT01367444, NCT01736592) and efficiently transduces cultured human
96 RPE (Pawan K. Shahi, 2019; Singh et al., 2013b). GFP expression was observed in ARB iPSC-RPE cells
97 starting one-week post-transduction (**Figure S3A**) and immunocytochemical (ICC) analysis confirmed
98 enhanced expression of BEST1 (**Figure S3B**). By ≥ 4 weeks post-LV transduction, CaCC current density
99 in ARB iPSC-RPE increased significantly, reaching levels comparable to WT iPSC-RPE (**Figure 2D,I,J;**
100 **Extended Figure 3C**). Furthermore, transduced monolayers of ARB iPSC-RPE demonstrated enhanced
101 degradation of rhodopsin following POS feeding (**Figure 2E**). These findings, together with those
102 reported by Guziewicz et al. (Guziewicz et al., 2018) and Li et al. (Li et al., 2017), support virus-mediated
103 *hBEST1* GA as a treatment for ARB.

104

105 ***BEST1* GA also restores CaCC activity and enhances POS degradation in iPSC-RPE derived from**
106 **some—but not all—adBD lines.**

107 Although not as intuitive, we also suspected that GA might be a viable solo therapeutic strategy
108 for a subset of adBD-causing mutations. Based on the eukaryotic BEST1 crystal structure, we
109 hypothesized that mutations affecting chloride or calcium ion binding sites would not affect gross
110 structure of the channel, but rather reduce its regulatory response and/or ion conductance capacity
111 proportional to the ratio of WT versus MT monomers. If so, we would expect increased CaCC activity
112 simply by shifting this ratio toward incorporation of more WT monomers through GA (**Figure 2F**).

113 Similar to ARB iPSC-RPE, CaCC activity in iPSC-RPE from all three adBD lines was diminished
114 compared to control (**Figure 2G (left); Figure S2C,E,F**). Single-cell patch clamp experiments on the
115 gene-corrected R218C>WT isogenic iPSC-RPE control showed CaCC current density at levels similar to
116 native WT control lines (**Figure S2D**), confirming that the diminished CaCC activity is indeed the result

117 of the mutation. The *hVMD2-hBEST1-T2A-GFP* LV construct was then used to transduce iPSC-RPE
118 from all three adBD patients (**Figure S3D**). At ≥ 4 weeks post-transduction, CaCC activity was restored in
119 iPSC-RPE containing mutations in a chloride (R218C) or calcium (N296H) binding site, whereas iPSC-
120 RPE harboring the A146K mutation, which resides in a structural domain of the channel, did not show
121 restoration of CaCC activity (**Figure 2G,I,J; Figure S3E-G**). Consistent with these single-cell
122 electrophysiological findings, GA improved rhodopsin degradation in R218C and N296H iPSC-RPE, but
123 not in A146K iPSC-RPE (**Figure 2H**).

124

125 **GE specifically disrupts the MT allele in adBD iPSCs and iPSC-RPE with high efficiency and**
126 **negligible off-target editing.**

127 To determine whether A146K iPSC-RPE would respond to an alternative therapeutic approach,
128 we tested GE as a means to eliminate expression of the MT *BEST1* allele (**Figure 3A**). GE with CRISPR-
129 Cas9 creates targeted double strand breaks in genomic DNA that are primarily repaired by endogenous
130 non-homologous end joining (NHEJ) (Cox et al., 2015), leading to insertion and deletion mutations
131 (indels). These indels can cause transcriptional frameshifts that lead to premature termination codons,
132 activation of intrinsic nonsense-mediated decay (NMD) pathways, and degradation of transcription
133 products (Popp and Maquat, 2016). Since we previously demonstrated successful targeting of the R218C
134 MT allele using sgRNAs (Steyer et al., 2018), sequences targeting the R218 locus in either the MT or the
135 WT allele were cloned into a LV plasmid that encoded both the sgRNA and a human codon optimized
136 *Streptococcus pyogenes Cas9 (spCas9)-T2A-reporter* transcript (**Figure 3B,C**).

137 Using these GE constructs, we first transduced both undifferentiated R218C adBD iPSCs and
138 gene-corrected, isogenic control, R218C>WT iPSCs. In R218C>WT iPSCs, we observed a dose-
139 dependent increase in percent edited alleles after GE treatment with LV encoding WT sgRNA, but no

140 editing after treating with LV encoding MT (R218C) targeted sgRNA (**Figure 3D left**). However, in
141 R218C iPSCs we observed editing after GE with both WT sgRNA and R218C sgRNA (**Figure 3D right**).
142 Similarly, GE of iPSC-RPE with R218C sgRNA revealed a dose dependent increase in editing in R218C
143 iPSC-RPE with minimal editing in R218C>WT iPSC-RPE (**Figure 3E**). Together, these results indicate
144 high specificity of the R218C sgRNA for the MT allele over the heterozygous WT allele. Observation of
145 minimal editing (1.6% max, ratio of MT:WT editing = 19.5; **Supplemental Data File A**) at the non-
146 targeted WT allele in iPSC-RPE, but not in undifferentiated iPSCs, may reflect open chromatin around
147 the actively transcribed *BEST1* locus in iPSC-RPE (Kuscu et al., 2014). Notably, an average of 95% of
148 the edited alleles in iPSC-RPE resulted in a frameshift mutation (**Figure 3F,G bottom; Supplemental**
149 **Data File A**), which is higher than the 70% frameshift rate observed in iPSCs (**Figure 3F,G top**) or
150 predicted using a recent machine learning algorithm (Shen et al., 2018) (**Supplemental Data File B**).

151 Next, we performed an off-target analysis after GE of R218C iPSCs (**Figure S4**) or R218C iPSC-
152 RPE (**Figure 3H**) with the R218C sgRNA. Analysis of the top nine off-target sites revealed measurable
153 off-target editing only at the second-ranked locus, which maps to an unannotated region on chromosome
154 7, 140 kb from any known transcription product. Conversely, we observed overall editing of $24.9\% \pm$
155 4.5% [SD] at the on-target (*BEST1*) locus in iPSC-RPE (**Figure 3H**). Due to high specificity of the
156 R218C sgRNA for the R218C allele, this equates to editing in approximately 50% of the MT alleles.

157 To evaluate for NMD, we quantified WT and MT (R218C + edited) sequencing reads from both
158 DNA and RNA isolated from iPSC-RPE cultures after GE (**Figure S5**). We observed a significant
159 increase in the ratio of WT to MT RNA in GE versus control groups; however, no such increase was
160 observed in the ratio of WT to MT DNA allele frequency between these groups (**Figure 3I**). Together,
161 these data indicate significant degradation of MT transcripts following GE, presumably through NMD.

162

163 **MT allele-specific GE restores CaCC activity in iPSC-RPE derived from all tested adBD lines with**
164 **no demonstrable change in the RPE transcriptional signature.**

165 We next assessed phenotypic rescue in control versus GE iPSC-RPE using LV vectors expressing
166 sgRNAs targeting specific alleles. Single-cell patch clamp experiments revealed restoration of CaCC
167 activity in R218C, N296H, and A146K iPSC-RPE cells (**Figure 3J-L; Figure S6**). Finally, to search for
168 off-target or other untoward transcriptional effects from GE, we performed single-cell RNA sequencing
169 (scRNA-seq) for 12,061 individual iPSC-RPE cells treated with GE. iPSC-RPE (R218C, N296H, A146K,
170 or gene-corrected R218C>WT) were edited with vectors encoding *spCas9-T2A-GFP* and either a MT
171 allele-targeted sgRNA or a control sgRNA targeting the *AAVSI* safe harbor locus (Sadelain et al., 2011),
172 to generate a total of eight separate samples (**Figure S7**).

173 Evaluation of t-Distributed Stochastic Neighbor Embedding (t-SNE) clustering of cells across all
174 eight samples indicated that, by virtue of using the *hVMD2* promoter, *spCas9-T2A-GFP* transcript levels
175 closely correspond with *BEST1* transcript levels (**Figure 3M**). Visual comparison of t-SNE clustering of
176 each individual sample demonstrated that transcriptional signatures are grossly similar between iPSC-
177 RPE lines whether treated with MT allele-targeted (+GE) or control (*AAVSI*) sgRNA (**Figure 3N top**).
178 This observation was supported quantitatively by non-negative matrix factorization (NMF). NMF analysis
179 demonstrated that greater transcriptome variation exists between iPSC-RPE from different lines than
180 between iPSC-RPE from the same line treated with MT allele-targeted or control sgRNA (**Figure S7B**).

181 Additional analysis of global gene expression (**Figure 3N bottom**) and of a focused set of genes
182 related to negative or off-target effects (including cell cycle regulation, apoptosis, DNA damage response,
183 or innate immune response; **Figure S7C**) did not reveal significant upregulation of those gene sets in MT
184 allele-targeted (+GE) versus control sgRNA-treated samples.

185

186 **DISCUSSION**

187 The observation that adBD mutations associated with ion binding may be amenable to GA greatly
188 expands the patient population that might benefit from this therapeutic approach. However, the stark
189 difference in functional response to GA among our adBD iPSC-RPE models underscores the need to vet
190 patients for GA candidacy carefully. The mechanism underlying selective GA responsivity in adBD is not
191 due to traditional allelic haploinsufficiency, in which half the normal amount of WT protein and no MT
192 protein is produced, resulting in fewer (but fully WT) BEST1 channels. Such a situation exists in parents
193 of ARB patients, who have no demonstrable disease phenotype. Rather, adBD MT monomers are
194 incorporated alongside WT monomers in all (or nearly all) BEST1 channels, resulting in ion binding site
195 insufficiency and channel impermeability, which is surmountable by WT *BEST1* GA. In contrast, we
196 hypothesize that *BEST1* mutations like A146K—which converts a nonpolar amino acid to a polar amino
197 acid in a structural region of the protein—has more pervasive functional consequences, resulting in
198 resistance to GA even at low MT:WT monomer ratios. Whether such mutations eventually can be
199 overcome by GA via increasing the expression levels of the WT transgene is yet to be determined.

200 There is precedence for using patient-specific iPSCs as preclinical efficacy models for gene
201 therapy (Vasireddy et al., 2013). Our work extends this capability by providing a framework for
202 preclinical testing of mutation-specific responses in a genotypically heterogenous disease. It remains to be
203 determined whether separate adBD iPSC-RPE models will be required to assess suitability of GA versus
204 GE for every mutation, or if a few models can sufficiently represent larger categories of mutations (*e.g.*,
205 ion binding sites or structural regions).

206 For adBD mutations like A146K that are not amenable to GA, we showed that targeted GE holds
207 promise as a future therapy. Importantly, we observed high efficiency out-of-frame editing in iPSC-RPE
208 compared to undifferentiated iPSCs. This result is consistent with recent reports of variable mutation bias

209 across different cell types (Shen et al., 2018), and points to the importance of evaluating GE using specific
210 cell type(s) targeted by disease, and not surrogate cell types. In addition, editing at *BEST1* in iPSC-RPE
211 did not provoke an increase in expression of genes associated with cell cycle regulation, apoptosis, DNA
212 damage response, or innate immune response in comparison to editing at a well characterized safe-harbor
213 locus (Sadelain et al., 2011) with a previously described sgRNA (Mali et al., 2013). This is in contrast to
214 studies in other cell types that have reported potential for Cas9-mediated GE to provoke undesirable
215 effects, including innate immune response (Wienert et al., 2018) and apoptosis, among other concerns
216 (Cromer et al., 2018).

217 Our results provide a blueprint to guide gene therapy choice in the era of GA and GE. With its
218 inherently larger target populations and established track record in patients, it is practical to utilize GA
219 when possible, reserving GE for mutations that require allele repair or knockout or are otherwise
220 untreatable by GA. It is noteworthy that the two adBD lines that demonstrated restoration of CaCC
221 activity with GA or GE did so with equal efficacy, underscoring the suitability of Best disease for either
222 approach. Other desirable characteristics of Best disease as a clinical candidate for GA or GE include 1) a
223 wide time window for gene therapy intervention, 2) accessibility of RPE using standard surgical
224 techniques, 3) a small (5.5 mm diameter) treatment area, 4) availability of noninvasive retinal imaging
225 and functional assessment tools, and 5) growing patient safety data from other RPE-based gene therapy
226 trials (Cukras et al., 2018; Lam et al., 2019; Russell et al., 2017). As such, Best disease is well-positioned
227 to become the first genotypically heterogeneous disorder with dominant and recessive inheritance patterns
228 to have a full menu of therapeutics for all affected individuals. Furthermore, implications of this work
229 likely extend beyond the eye and Best disease to other intractable monogenic conditions caused by
230 mutations in multimeric ion channels, including congenital myasthenic syndromes and some forms of
231 epilepsy (George, 2004; Schaaf, 2014; Villa and Combi, 2016).

232

233 **ACKNOWLEDGEMENTS**

234 The authors thank Alfred Lewin (U. Florida) for the *hVMD2-hBEST1-T2A-GFP* plasmid construct; the
235 Cellular Imaging and Analysis core at the University of Wisconsin-Madison Waisman Center; Budd
236 Tucker and Ed Stone (U. Iowa) for providing the ARB iPSC line, corresponding Scorecard data, and ARB
237 patient fundus images; and Andrew Thliveris for helpful discussions. This work was supported by NIH
238 R01EY024588, Foundation Fighting Blindness, Research to Prevent Blindness, Retina Research
239 Foundation Emmett Humble Chair, and McPherson Eye Research Institute Sandra Lemke Trout Chair in
240 Eye Research (to D.M.G.); NSF CBET-1350178 and CBET-1645123, NIH R35GM119644, John Merck
241 Fund Translational Research Program, Brain & Behavior Research Foundation, Burroughs Wellcome
242 Fund (to K.S.); NIH R01EY024995 and Retina Research Foundation M.D. Mathews Professorship (to
243 B.R.P.); NIH T32HG002760 and F30EY027699, VitreoRetinal Surgery Foundation (to B.S.); DGE-
244 1747503 (to K.M.). This study was supported in part by a core grant to the Waisman Center (NICHD
245 U54 HD090256). We thank members of the Gamm and Saha labs for comments on the manuscript,
246 plasmid depositors to Addgene, the University of Wisconsin-Madison Biotechnology Center for DNA
247 sequencing, and the University of Wisconsin-Madison Skin Disease Research Center for assistance with
248 virus preparation.

249

250 **AUTHOR CONTRIBUTIONS**

251 D.S. and D.M.G. designed the GA experiments. B.S., D.S., D.M.G. and K.S. designed the GE
252 experiments. P.K.S. and B.R.P. performed and analyzed the electrophysiology experiments. D.S. and B.S.
253 performed all other experiments with contributions from R.V., K.L.E., C.B, S.S.S., A.A., and E.C. K.M.,
254 S.S., V.P., A.F.S., and S.R. were primarily responsible for the scRNA-seq analysis. D.S., B.S., K.S., and

255 D.M.G. wrote the manuscript and analyzed data with input from all authors. D.M.G., K.S., and B.R.P.
256 supervised research.

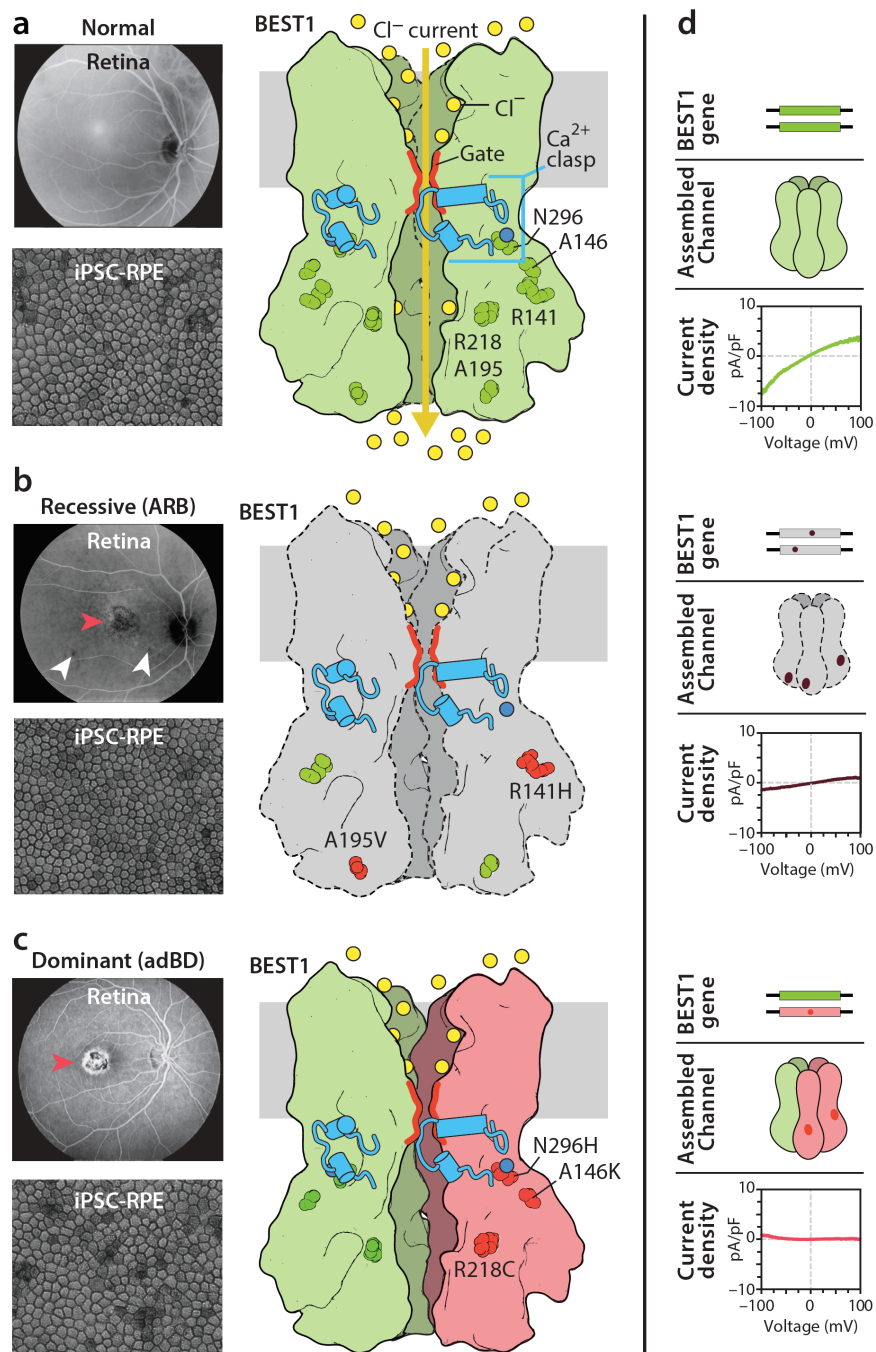
257

258 **COMPETING INTERESTS STATEMENT**

259 The authors declare no competing interests.

260 FIGURES AND FIGURE LEGENDS

261 Figure 1

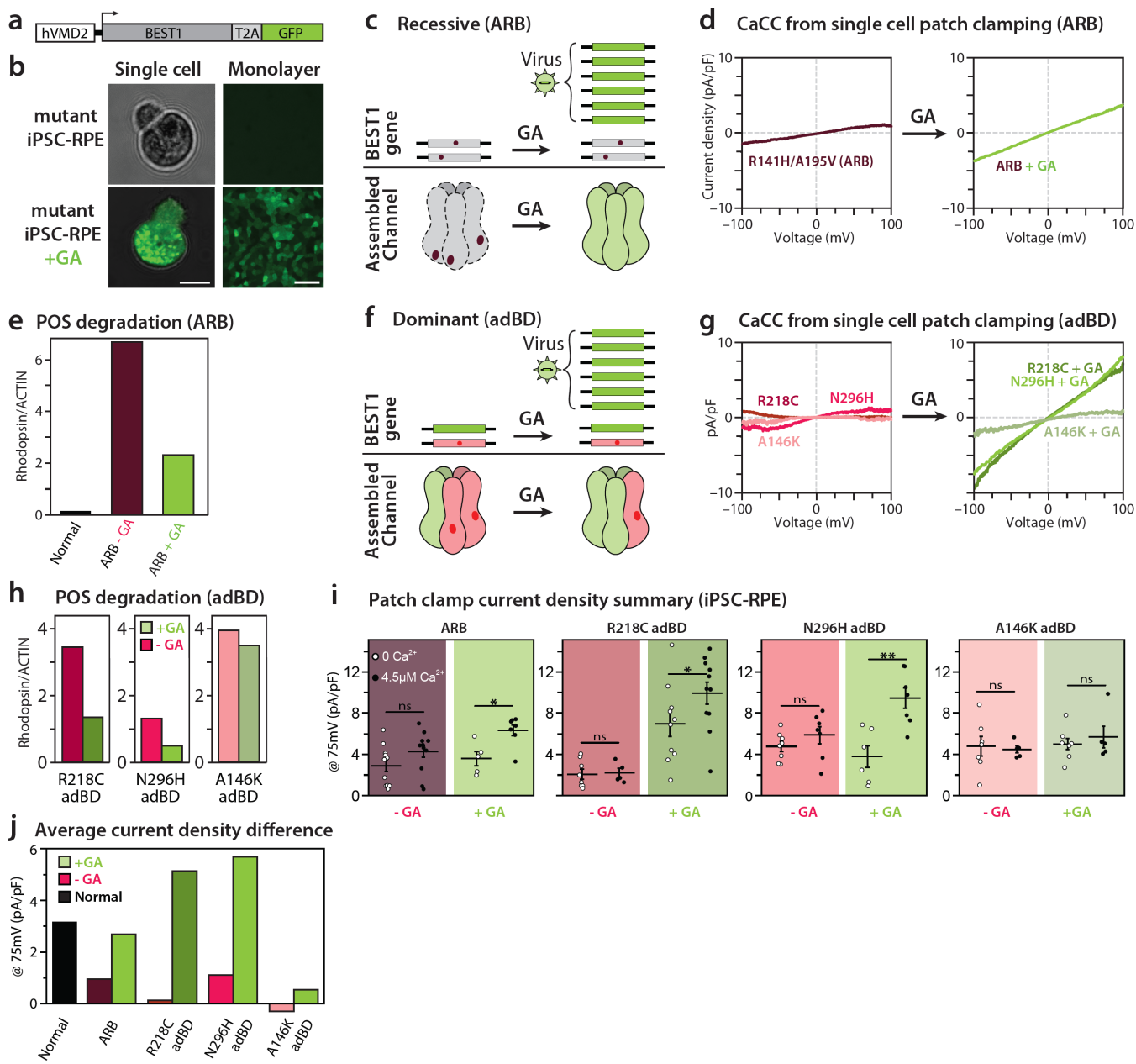


262

263

264 **Figure 1 | BEST1 mutations reduce CaCC current in Best disease iPSC-RPE. (A)** Images (in
265 grayscale) of a normal fundus (*top*) and control (WT) iPSC-RPE (*bottom*). A fully functional homo-
266 pentameric BEST1 channel is formed by expression and assembly of WT alleles and subunits (*green*),
267 respectively, allowing movement of chloride ions (*yellow circles*) upon binding of calcium ions (*blue*
268 circle) (based on eukaryotic BEST1 crystal structure by Dickson et al. (Dickson et al., 2014)). **(B)** *Top*,
269 Fundus image of an ARB patient with R141H/A195V compound heterozygous mutations in *BEST1*
270 showing a vitelliform lesion in the macula (*red arrowhead*) as well as small lesions outside the macula
271 (*white arrowheads*), which is characteristic of ARB. *Bottom*, iPSC-RPE derived from the same ARB
272 patient. Pentameric channel assembly for these mutations is expected to be significantly reduced due to
273 protein degradation (denoted by *gray* subunits with dashed outlines). **(C)** *Top*, Fundus image showing a
274 vitelliform macular lesion (*red arrowhead*) in an adBD patient with a heterozygous R218C mutation in
275 *BEST1*. *Bottom*, iPSC-RPE derived from the same adBD patient. Both adBD mutant (MT) (*red*) and WT
276 (*green*) monomers are assembled in the pentameric channel. **(D)** CaCC current density-voltage plots from
277 WT (*top*), R141H/A195V ARB (*middle*), or R218C adBD (*bottom*) iPSC-RPE cells, as determined by
278 calculating the difference in average chloride currents in the presence or absence of calcium (**Figure S2**).
279 For +calcium: n = 6 cells for WT, 12 cells for R141H/A195V ARB, and 5 cells for R218C adBD; for no
280 calcium: n = 8 cells for WT, 12 cells for R141H/A195V ARB, and 8 cells for R218C adBD (data
281 combined from at least two replicates). The number of cells from each replicate is listed in **Table S8**. See
282 also Figures S1-S3.

283 **Figure 2**



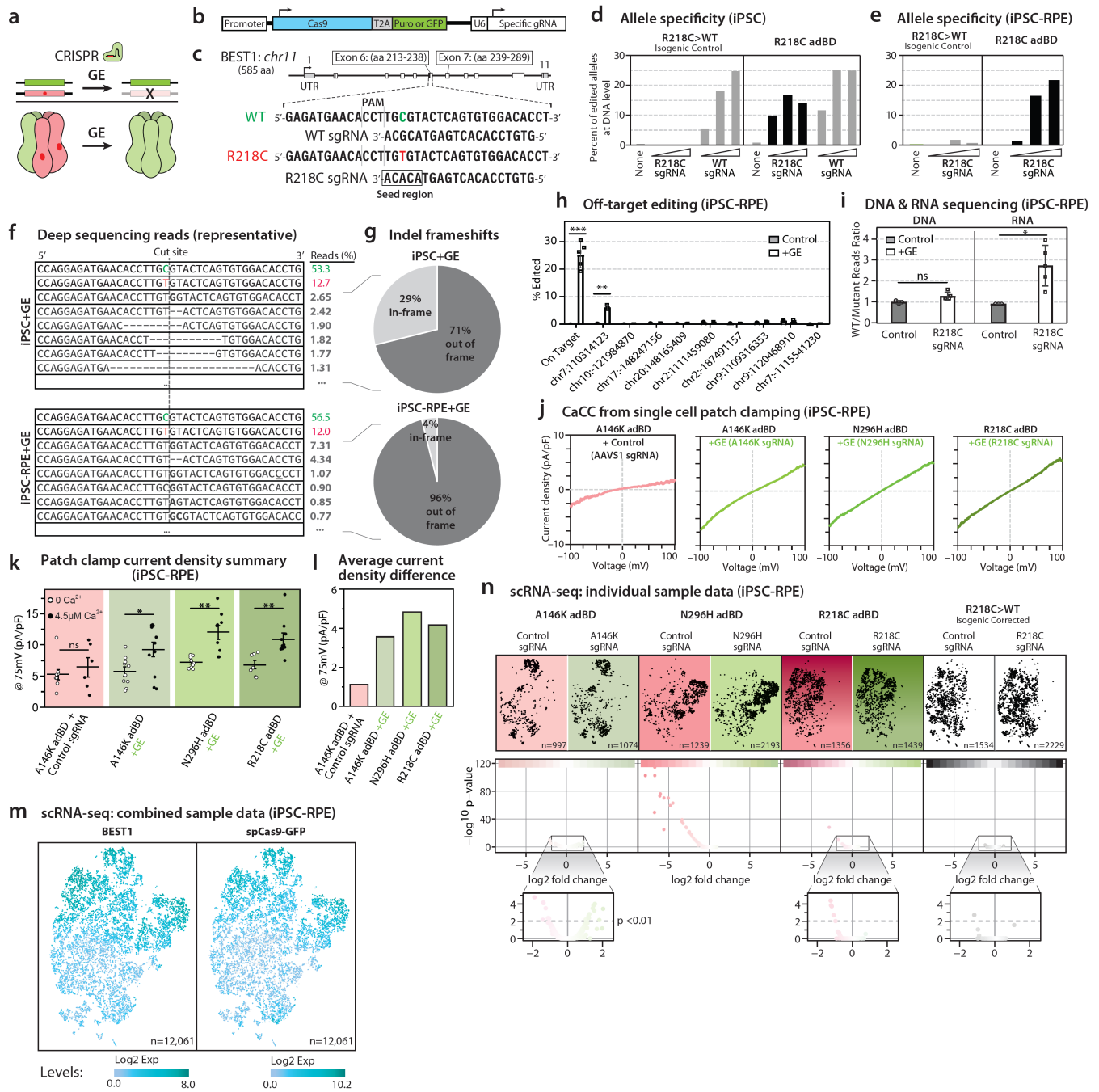
284

285

286 **Figure 2 | Mutation-dependent rescue of Best disease phenotypes by gene augmentation (GA).** (A)
287 Construct used for BEST1 GA. (B) Presence or absence of GFP fluorescence in dissociated iPSC-RPE
288 cells (*left*) or iPSC-RPE monolayers (*right*) before (*top*) or after (*bottom*) GA. Scale bar = 10 μm (*left*); 50
289 μm (*right*). (C) Rationale for GA in ARB: LV-mediated expression of WT hBEST1 (*green* subunits) will
290 compensate for the lack of endogenous BEST1 expression (*gray* subunits) and increase formation of fully
291 functional homo-pentameric BEST1 channels. (D) CaCC current density-voltage plots before (*left*) and
292 after (*right*) GA of ARB iPSC-RPE. CaCC current density-voltage plot of ARB (-GA) is the same as
293 shown in Figure 1d, and is included for comparison. For the ARB+GA condition, $n = 7$ cells for +calcium
294 and 5 cells for no calcium (data combined from two replicates). The number of cells from each replicate is
295 listed in **Table S8**. (E) Rhodopsin levels 120 hr after POS feeding in WT, ARB, and ARB+GA iPSC-
296 RPE. The Western blot used for quantifying rhodopsin levels is shown in **Figure 2**. (F) Rationale for
297 using GA in adBD: LV-mediated expression of WT hBEST1 (*green* subunits) will increase the ratio of
298 WT:MT (*green:red* subunits) BEST1 monomers, thus improving channel function. (G) CaCC current
299 density-voltage plots before (*left*) or after (*right*) GA of adBD iPSC-RPE. Before GA (*left* panel): for
300 +calcium: $n = 7$ cells for N296H and 5 cells for A146K adBD; for no calcium: $n = 8$ cells for N296H and
301 7 cells for A146K (data combined from two replicates). The CaCC current density-voltage plot for R218C
302 adBD (-GA) is the same as shown in Figure 1d, and is included for comparison. After GA (*right* panel):
303 for +calcium: $n = 11$ cells for R218C, 7 cells for N296H, and 5 cells for A146K; for no calcium: $n = 9$
304 cells for R218C, 6 cells for N296H, and 8 cells for A146K (data combined from two replicates). The
305 number of cells from each replicate is listed in **Table S8**. (H) Rhodopsin levels 48 hours after feeding
306 POS to adBD iPSC-RPE with or without GA. Western blots used for quantifying rhodopsin levels are
307 shown in **Data S2**. (I) CaCC conductance for individual iPSC-RPE cells, and (J) mean CaCC

308 conductance at 75 mV before or after GA. The number of cells is the same as for panels d and g. Error
309 bars in 2i represent mean \pm SEM; ns = $p \geq 0.05$, * for $p < 0.05$, ** for $p < 0.01$. See also Figures S1-S3.

310 **Figure 3**



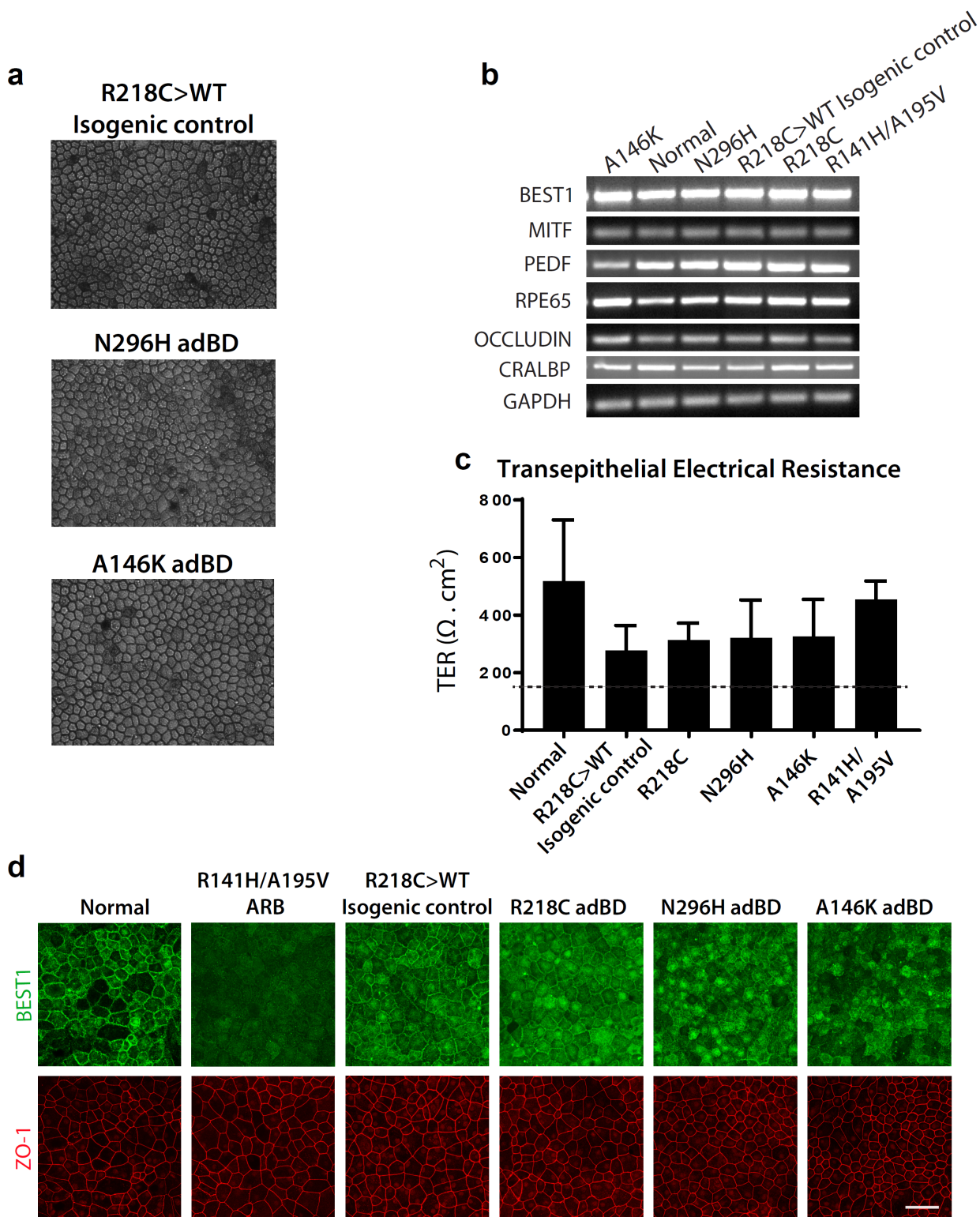
311

312

313 **Figure 3 | Gene editing (GE) rescues CaCC activity in all adBD iPSC-RPE. (A)** Rationale for using
314 GE in adBD: introducing out-of-frame indels specifically in the MT *BEST1* allele via CRISPR/Cas9
315 targeting can silence its expression and restore normal WT BEST1 channel function. **(B)** LV construct
316 used to express *spCas9* and MT allele-targeted sgRNAs. **(C)** Diagram showing the heterozygous base pair
317 substitution in R218C adBD (indicated in *red* and *green*) and design of the R218C and WT sgRNAs. **(D)**
318 Percent of edited alleles in R218C>WT isogenic control iPSCs and R218C adBD iPSCs with increasing
319 concentrations of WT sgRNA LV (single replicate at 0, 10, 100, or 500 μ l dose). **(E)** Percent of edited
320 alleles after treatment of R218C>WT isogenic control and R218C adBD iPSC-RPE with R218C sgRNA
321 LV (single replicate at 0, 5, 50, or 150 μ l dose). **(F)** Deep sequencing reads after treatment of R218C
322 iPSC (*top*) or R218C iPSC-RPE (*bottom*) with R218C sgRNA LV and **(G)** corresponding calculated indel
323 frameshift frequency for R218C iPSCs (*top*) and R218C iPSC-RPE (*bottom*). For panels f and g, data
324 from a single representative example is shown; for additional replicates see **Supplemental Data File A**.
325 **(H)** Frequency of edited alleles at on-target and top nine ranked off-target loci in iPSC-RPE treated with
326 R218C sgRNA LV (n=3 for control and n=5 for +GE, except n=3 at *chr 7* locus). **(I)** Ratio of WT to MT
327 allele DNA (*left*) and mRNA transcript reads (*right*) from R218C iPSC-RPE cultures treated with R218C
328 sgRNA LV (n=5) or control LV (n=3 for *AAVSI* sgRNA and no sgRNA LV). **(J)** CaCC current density-
329 voltage plots from single-cell patch clamp experiments of iPSC-RPE treated with MT allele-targeted
330 sgRNA LV. For +calcium: n = 6 cells for *AAVSI*, n = 11 cells for A146K, n = 10 cells for R218C, n = 9
331 cells for N296H; for no calcium: n = 9 cells for *AAVSI*, n = 10 cells for A146K, n = 7 cells for R218C, n
332 = 9 cells for N296H (data combined from two replicates). The number of cells from each replicate is
333 listed in **Table S8**. **(K)** CaCC conductance for individual iPSC-RPE cells, and **(L)** mean CaCC
334 conductance at 75 mV. The number of cells is the same as for panel j. **(M)** t-SNE plot of single iPSC-RPE
335 cells across all 8 samples with relative expression of *BEST1* (*left*) and *spCas9-T2A-GFP* (*right*) depicted

336 via increasing shades of *blue*. Total number of cells analyzed (n) is shown. **(N)** *Top*, t-SNE plot of single
337 cells (*black* dots) from each treated sample. Number of cells analyzed (n) for each sample is shown.
338 *Bottom*, Volcano plots of transcriptome-wide differences in expression of individual genes (*red* or *green*
339 dots) between iPSC-RPE of the same genotype treated with MT allele-targeted sgRNA (*green*) versus
340 control (*AAVS1*, *red*) sgRNA LV. $p < 0.01$ was the threshold for determining significant versus non-
341 significant changes in gene expression. Error bars in 3i represent mean \pm SD; ns = $p \geq 0.05$, * for $p < 0.05$,
342 ** for $p < 0.01$, *** for $p < 0.001$. Error bars in 3k represent mean \pm SEM. See also Figures S4-S7.

343 **Figure S1. Related to Figures 1-2.**

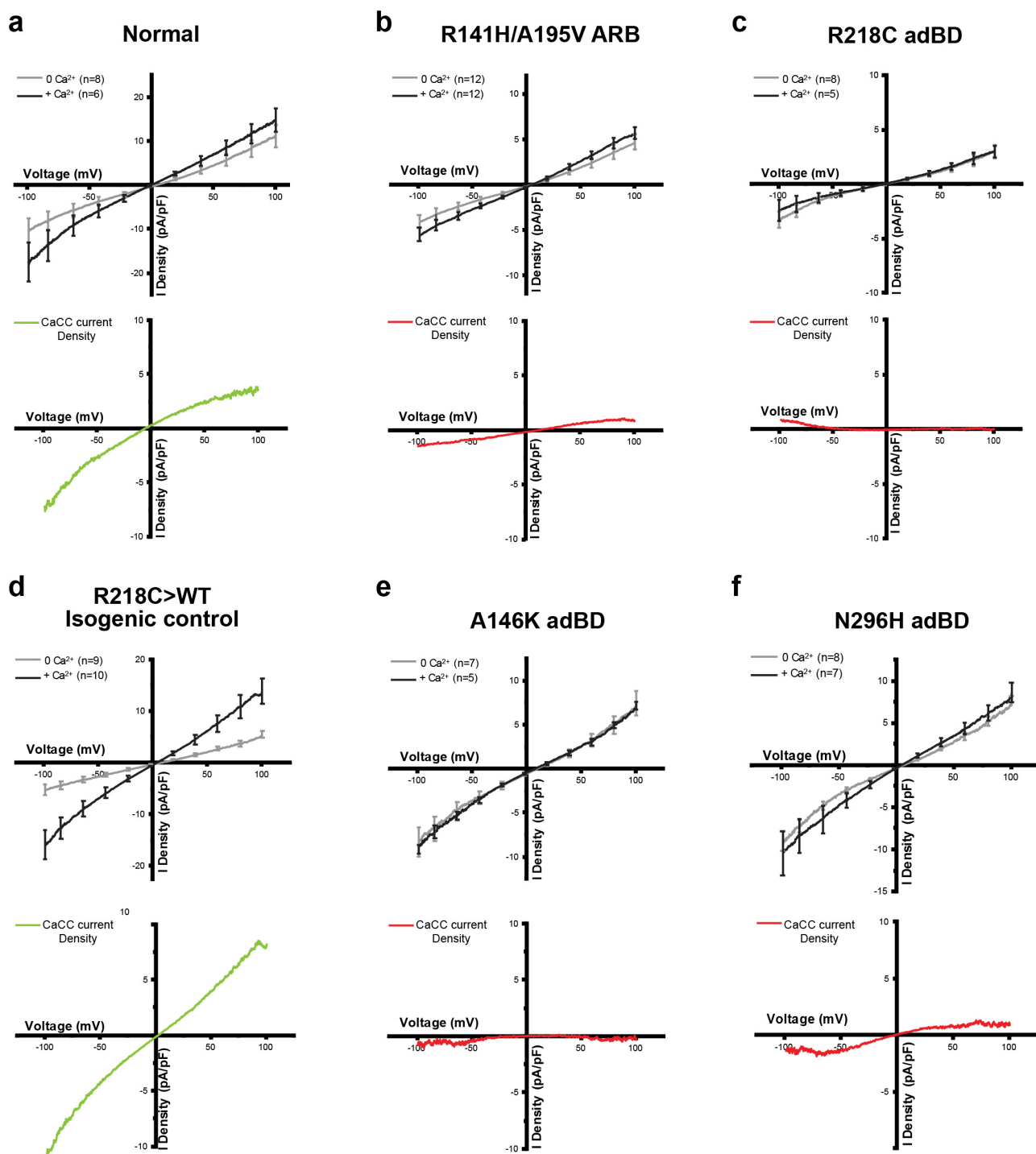


344

345

346 **Figure S1 | Characterization of iPSC-RPE. (A)** RPE differentiated from R218C>WT control iPSCs
347 (isogenic to the R218C adBD line) or patient-specific iPSCs harboring adBD mutations. **(B)** Gene
348 expression analysis (RT-PCR) of selected RPE-specific markers in all six lines. **(C)** Net transepithelial
349 electrical resistance (TER) ($\Omega \cdot \text{cm}^2$) for iPSC-RPE from all six lines. The dashed line demarcates the
350 minimum expected TER ($150 \Omega \cdot \text{cm}^2$). n=12 for each line (4 transwells from 3 replicates each), error bars
351 represent mean \pm SD. **(D)** BEST1 and ZO-1 expression in iPSC-RPE. BEST1 expression level in
352 R141H/A195V ARB iPSC-RPE is reduced compared to other lines. BEST1 was visualized in the far-red
353 channel but was pseudo-colored green. Scale bar = 50 μM and applies to all images in panel d.

354 **Figure S2. Related to Figures 1-2.**

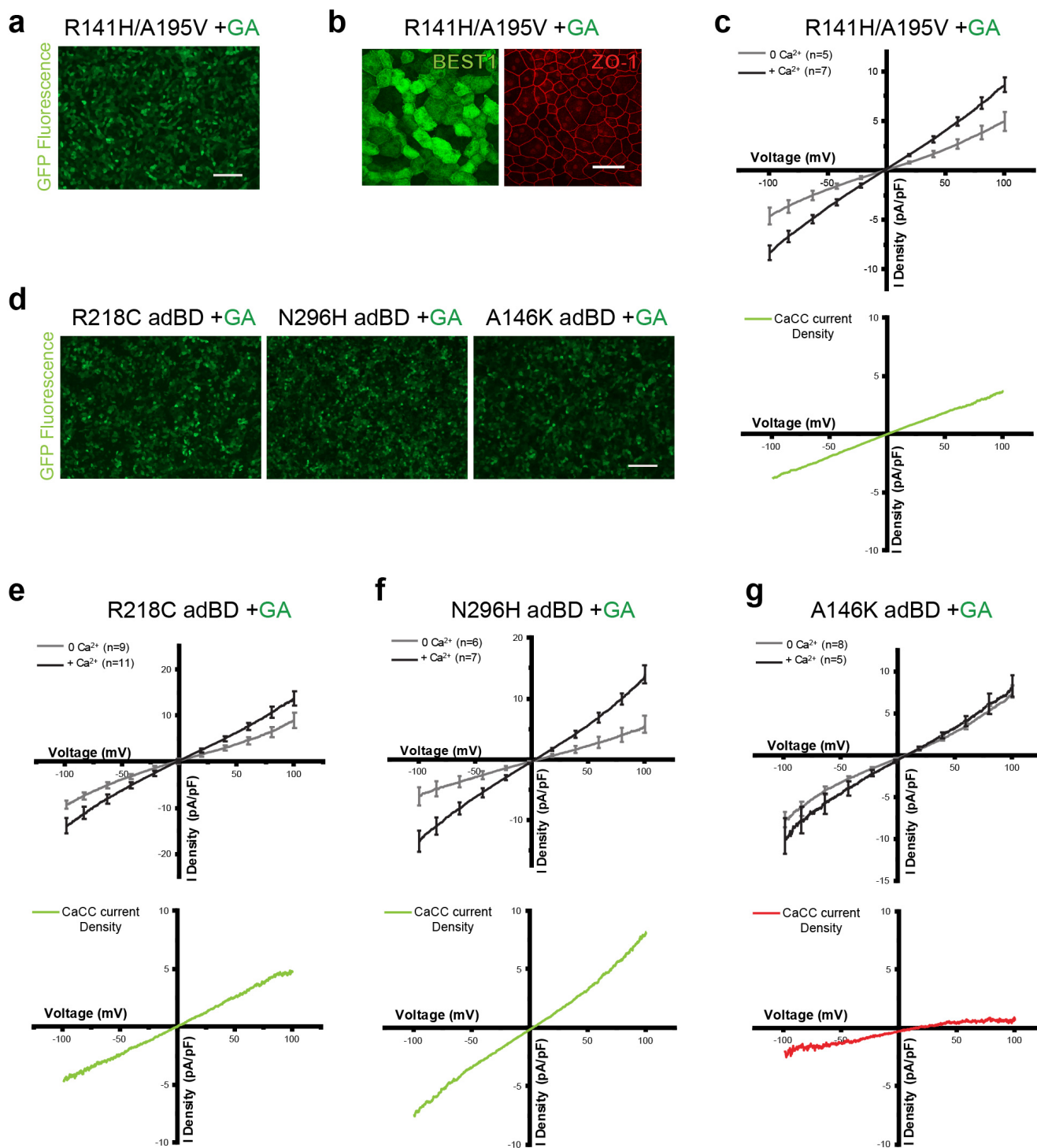


355

356

357 **Figure S2 | Measurement of CaCC activity in WT, ARB, adBD, and gene-corrected iPSC-RPE. (A-**
358 **C)** Chloride current traces, measured in the presence (*black*) or absence (*gray*) of calcium over a voltage
359 ramp (-100 to +100 mV), that were used to generate CaCC current density plots in Figure 1d (CaCC
360 current density traces are also shown here for each panel). **(D-F)** Chloride current traces measured in the
361 presence (*black*) or absence (*gray*) of calcium (*top*) and respective calculated CaCC current density traces
362 (*bottom*) for R218C>WT isogenic control, A146K adBD, and N296H adBD iPSC-RPE. 4.5 μ M calcium
363 was used for +calcium conditions. *Green* traces denote normal, while *red* traces denote reduced CaCC
364 current density. The number (n) of individual cells patch clamped in the presence or absence of calcium in
365 order to calculate CaCC current densities is shown in the top left corner of each graph. Data were
366 obtained from at least two replicates, and the n for each replicate is listed in **Table S8**.

367 **Figure S3. Related to Figures 1-2.**

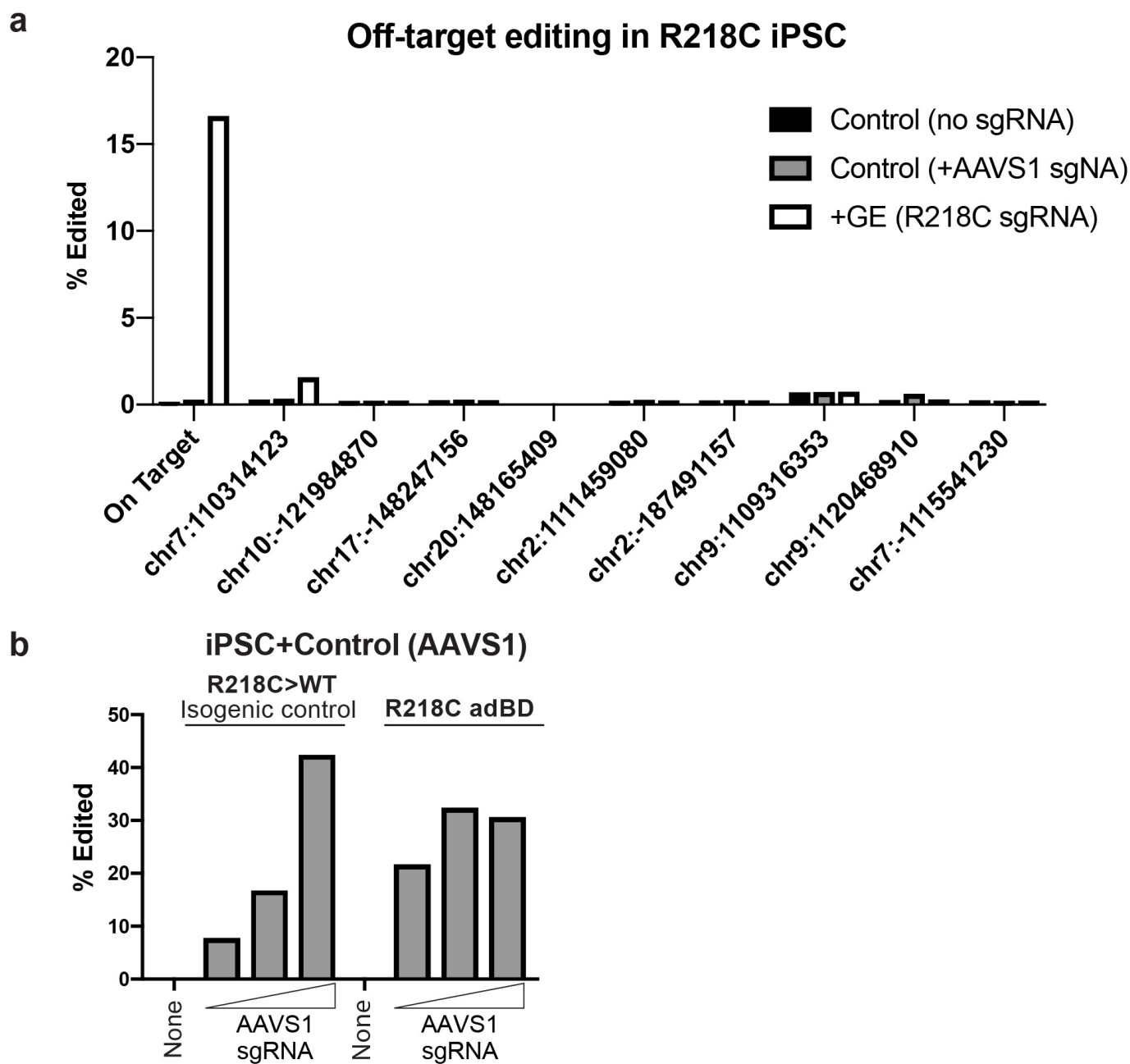


368

369

370 **Figure S3 | GA restores CaCC function in ARB iPSC-RPE and N296H and R218C adBD iPSC-**
371 **RPE, but not in A146K adBD iPSC-RPE. (A)** GFP fluorescence in R141H/A195V ARB iPSC-RPE
372 transduced with LV expressing hBEST1. Scale bar = 100 μ m. **(B)** ICC analysis of BEST1 and ZO-1
373 expression in R141H/A195V iPSC-RPE transduced with LV expressing hBEST1. Increased BEST1
374 expression is observed in R141H/A195V +GA cells. Scale bar = 50 μ m (applies to both images). **(C) Top,**
375 Chloride current traces of R141H/A195V iPSC-RPE after GA measured in the presence (*black*) or
376 absence (*gray*) of calcium. *Bottom,* Calculated CaCC current density trace for R141H/A195V iPSC-RPE
377 after GA (also shown in Figure 2d). **(D)** GFP fluorescence in adBD iPSC-RPE transduced with LV
378 expressing hBEST1. Scale bar = 100 μ m (applies to all three images). **(E-G) Top,** Chloride current traces,
379 measured in the presence (*black*) or absence (*gray*) of calcium over a voltage ramp (-100 to +100 mV),
380 that were used to obtain CaCC current density plots (*bottom*; also shown in Figure 2g). 4.5 μ M calcium
381 was used for +calcium conditions. *Green* traces represent restored CaCC current densities, while *red*
382 traces indicate no change. Cells with green fluorescence were used for all patch clamp measurements after
383 GA. The number (n) of individual cells patch clamped in the presence or absence of calcium in order to
384 calculate CaCC current densities is shown in the top left corner of each graph. Data were obtained from at
385 least two replicates, and the n for each replicate is listed in **Table S8**.
386

387 **Figure S4, Related to Figure 3.**

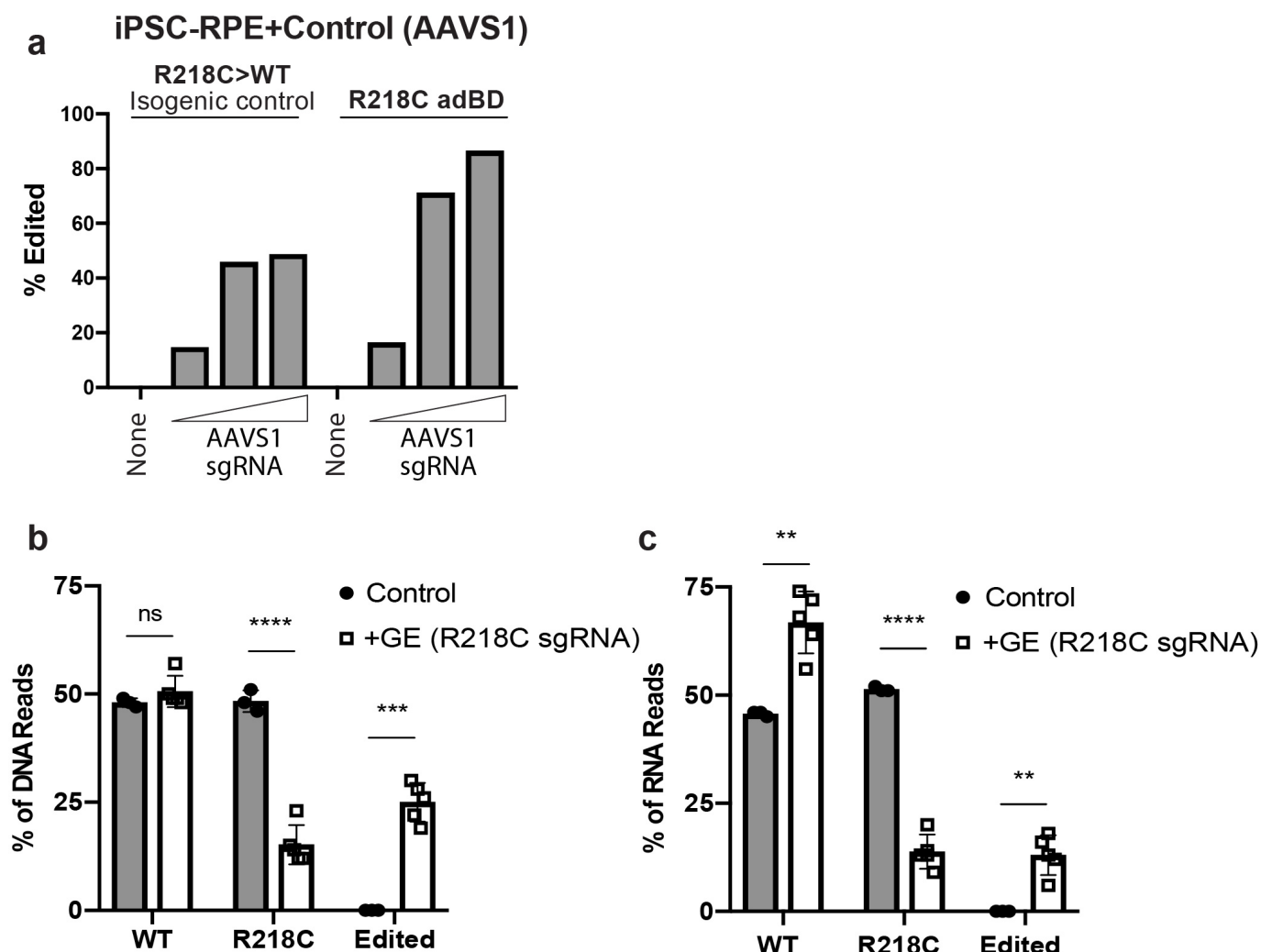


388

389

390 **Figure S4 | Quantification of off-target editing and *AAVS1* (control) editing in iPSCs. (A)** Percent of
391 alleles edited (% Edited) in R218C iPSCs at the on-target and top nine ranked off-target loci for the
392 R218C sgRNA LV. Data presented are for a single sequencing replicate (n=1 each) of untreated R218C
393 adBD iPSCs (no sgRNA) or R218C adBD iPSCs treated with LV encoding either R218C sgRNA or
394 *AAVS1* sgRNA. **(B)** Percent of *AAVS1* alleles edited (% Edited) in R218C iPSCs and R218C>WT
395 isogenic control iPSCs transduced with *AAVS1* sgRNA LV at 0, 10, 100, or 500 μ l dose.
396

397 **Figure S5, Related to Figure 3.**

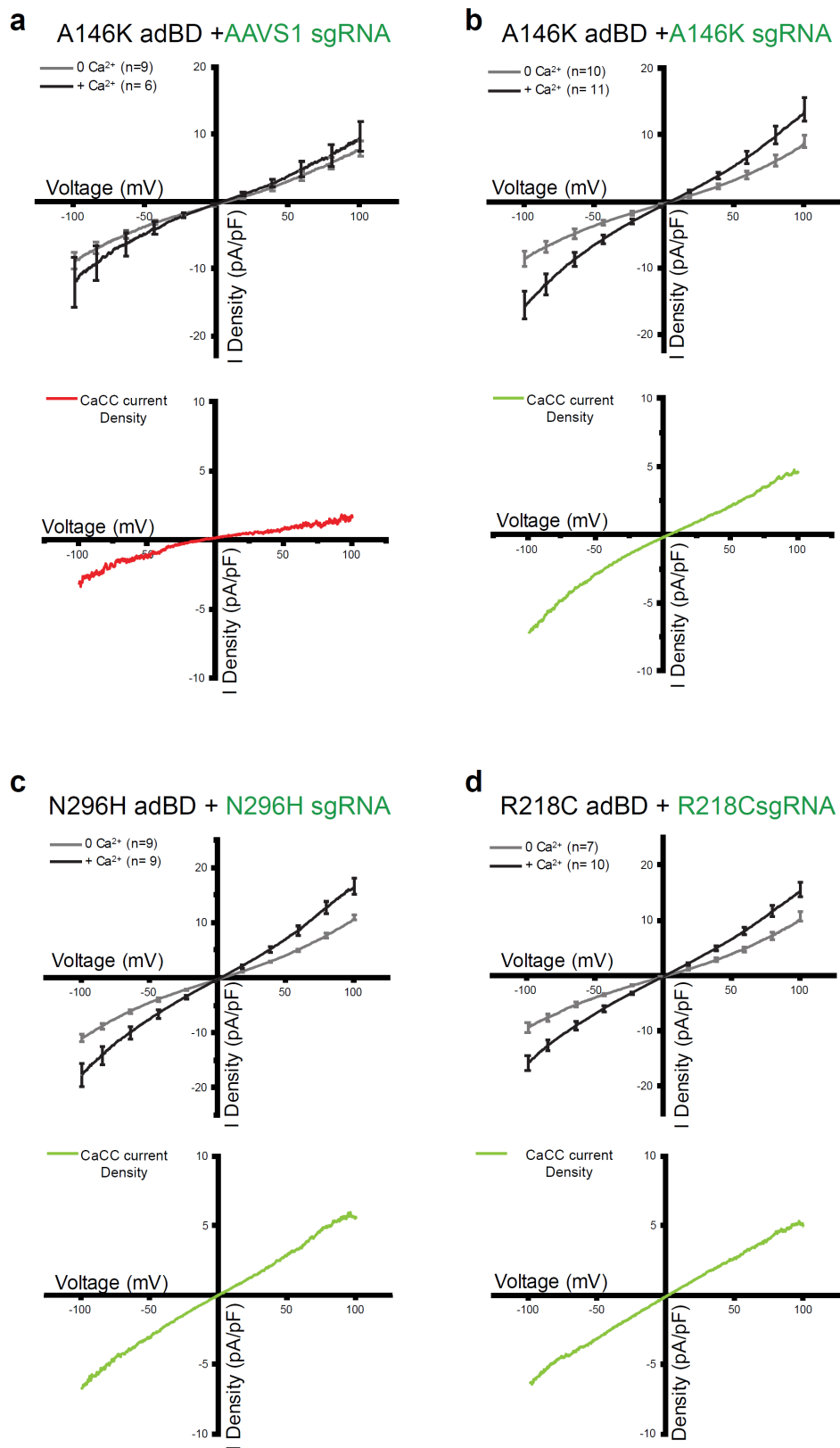


398

399

400 **Figure S5 | Quantification of DNA and RNA sequencing reads in GE iPSC-RPE. (A)** Percent of
 401 *AAVS1* alleles edited (% Edited) in R218C adBD iPSC-RPE and R218C>WT isogenic control iPSC-RPE
 402 transduced with *AAVS1* sgRNA LV at 0, 5, 50, or 150 μ l dose. **(B)** Percent of WT, unedited R218C, or
 403 edited DNA reads in R218C iPSC-RPE treated with R218C sgRNA or control (*AAVS1* sgRNA or no
 404 sgRNA) LV shown in Figure 3i. **(C)** Percent of WT, unedited R218C, or edited RNA reads corresponding
 405 to panel b and Figure 3i. Error bars represent mean \pm SD; ns = $p \geq 0.05$, * for $p < 0.05$, ** for $p < 0.01$, ***
 406 for $p < 0.001$, **** for $p < 0.0001$.

407 **Figure S6, Related to Figure 3.**

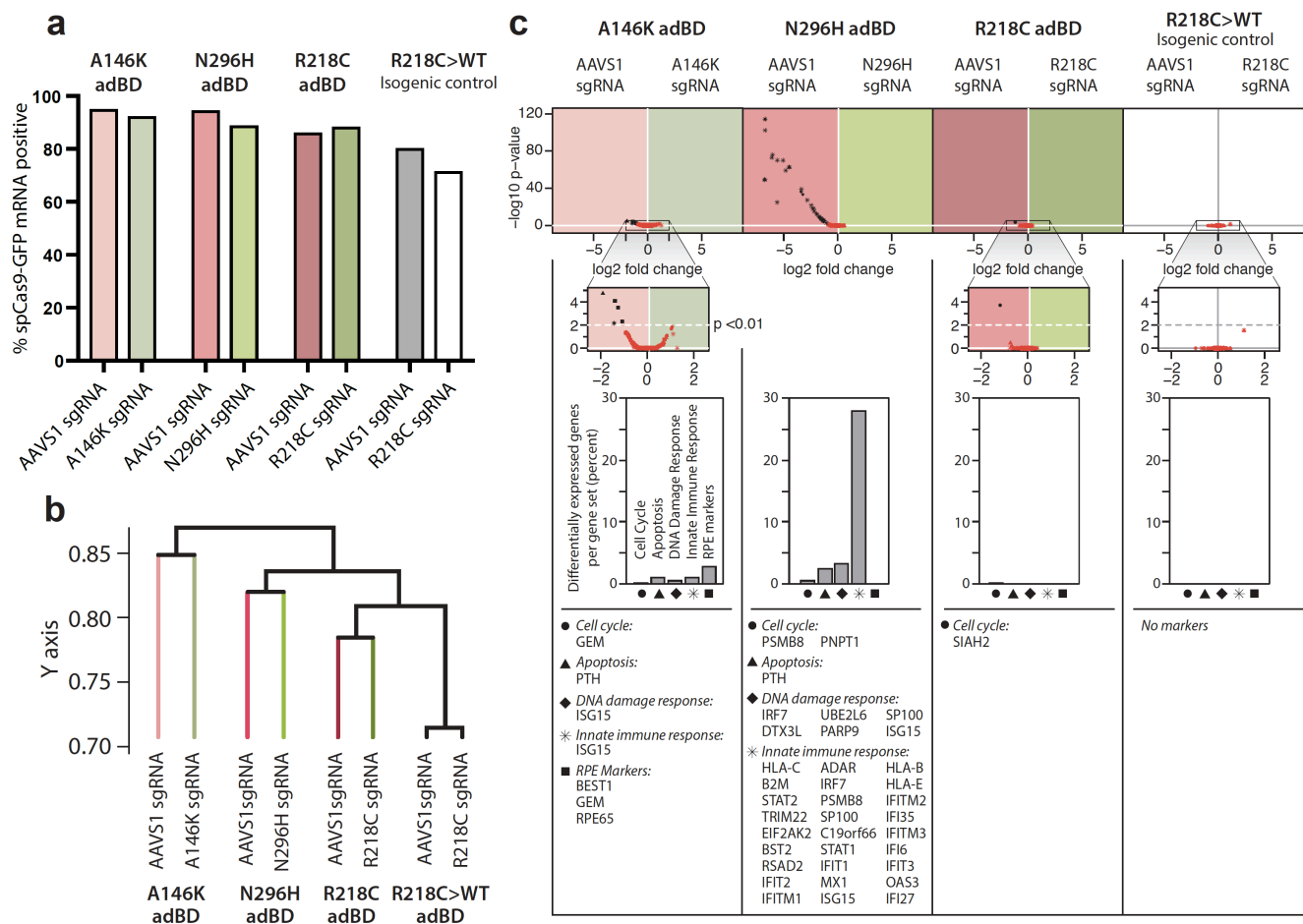


408

409 **Figure S6 | GE restores CaCC activity in iPSC-RPE from all adBD lines.** Chloride current traces
410 (*top*), measured in the presence (*black*) or absence (*gray*) of calcium over a voltage ramp (-100 to +100
411 mV), that were used to calculate CaCC current density plots (*bottom*) after GE of iPSC-RPE from each
412 adBD line. CaCC current density plots are also shown in Figure 3j. iPSC-RPE was edited using sgRNAs
413 targeting **A**, *AAVSI* site in A146K adBD iPSC-RPE, **B**, A146K mutation in A146K adBD iPSC-RPE, **C**,
414 N296H mutation in N296H adBD iPSC-RPE, or **D**, R218C mutation in R218C adBD iPSC-RPE. Cells
415 with GFP fluorescence were used for whole cell patch clamp measurements and 4.5 μ M calcium was used
416 for +calcium conditions. *Red* traces denote reduced CaCC current density, while *green* traces denote
417 restored CaCC function. The number (n) of individual cells patch clamped with or without calcium is
418 shown at the top left corner of each graph. Data were obtained from two replicates, and the n for each
419 replicate is listed in **Table S8**.

420

421 **Figure S7, Related to Figure 3**



422

423

424 **Figure S7 | Single-cell RNA-seq (scRNA-seq) analysis of iPSC-RPE after GE. (A)** Percent of analyzed
425 cells per sample for which *spCas9-T2A-GFP* transcripts were captured using scRNA-seq. **(B)**
426 Dendrogram tree depicting relative similarity between samples. Non-negative matrix factorization-based
427 gene cluster comparison across samples indicates that greater transcriptional variability exists between
428 iPSC-RPE lines than between the same iPSC-RPE line treated with LV vectors encoding *spCas9*, GFP, or
429 sgRNA (*AAVSI* sgRNA versus *BEST1* MT allele-targeted sgRNA). The dendrogram tree shows the
430 similarity of the transcriptomes from each sample, derived from the average Jaccard coefficient between
431 gene clusters from one sample and those from another sample. The y-axis denotes 1-average Jaccard
432 coefficient and indicates the distance between different samples (tree tips) as well as between groups of
433 samples (internal nodes). **(C)** Differential gene expression in 5 curated gene sets associated with cell cycle
434 regulation (*circles*), apoptosis (*triangles*), DNA damage response (*diamonds*), innate immune response
435 (*asterisks*), or RPE-identity (*squares*) in control (*AAVSI*) sgRNA versus MT allele-targeted sgRNA
436 treated samples. For one sample pair (N296H iPSC-RPE), genes associated with a potential adverse
437 treatment effect were upregulated in control sgRNA-treated sample compared to the MT allele-targeted
438 sgRNA-treated sample.
439

440 **STAR ★ METHODS**

441

442 **CONTACT FOR REAGENT AND RESOURCE SHARING**

443 Further information and requests for resources and reagents should be directed to and will be fulfilled by
444 the Lead Contact, David Gamm (dgamm@wisc.edu).

445

446 **EXPERIMENTAL MODEL AND SUBJECT DETAILS**

447 **iPSC lines**

448 A total of 6 iPSC lines, 2 control and 4 patient-specific, were used in this study. In addition to two
449 adBD patient-specific iPSC lines previously used by our group for Best disease modeling (Singh et al.,
450 2013b), we used three new iPSC lines (for detailed information on lines, including their characterization,
451 please refer to **Table S1**). Two of the new iPSC lines harbored patient specific mutations: R218C for
452 adBD and R141H/A195V for ARB. The ARB iPSC line was provided by Budd Tucker and Ed Stone
453 (University of Iowa). One isogenic control iPSC line was obtained by CRISPR/Cas9-based gene
454 correction of the patient-specific R218C adBD iPSC line (Steyer et al., 2018). All iPSC lines were
455 cultured either on mouse embryonic fibroblasts (MEFs) or on Matrigel. Lines cultured on MEFs were
456 maintained using iPS media (Dulbecco's Modified Eagle's Medium (DMEM)/F12 (1:1), 20% Knockout
457 Serum Replacement (KOSR), 1% MEM non-essential amino acids, 1% L-glutamine, 0.2 mM β -
458 mercaptoethanol, 100 ng/ml FGF-2), and iPSCs cultured on Matrigel were cultured with either mTeSR1
459 or StemFlex media. MEFs, FGF-2, and Matrigel were purchased from WiCell (Madison, WI). All other
460 cell culture reagents were purchased from ThermoFisher Scientific. Karyotyping were performed as a
461 quality control. The manuscript does not contain human subject or animal studies, and all work with iPSC

462 lines was carried out in accordance with institutional, national, and international guidelines and approved
463 by the Stem Cell Research Oversight Committee at the University of Wisconsin-Madison.

464

465 **METHOD DETAILS**

466 **Differentiation of iPSC lines to RPE**

467 Differentiation of iPSCs to RPE was performed as previously described (Singh et al., 2013a;
468 Singh et al., 2013b). Briefly, iPSCs were enzymatically lifted (1 mg/ml dispase for cells cultured on
469 MEFs; 2 mg/ml dispase or 1 ml ReLeSR for cells cultured on Matrigel) to form aggregates, also referred
470 to as embryoid bodies (EBs). EBs were maintained in suspension culture either in EB media (iPS media
471 without FGF-2) and then switched to neural induction media (NIM) on day 4, or gradually weaned off
472 mTeSR1/StemFlex and transitioned to NIM by day 4. NIM is composed of 500 ml DMEM/F12 (1:1), 1%
473 N2 supplement, 1% MEM non-essential amino acids, 1% L-glutamine, 2 µg/ml heparin. EBs were plated
474 on laminin (Cat# 23017015) coated 6-well plates (Nunc; Thermo Fisher Scientific) on day 7. On day 16,
475 neural rosettes were mechanically lifted, leaving adherent cells behind that were maintained in retinal
476 differentiation media (RDM; DMEM:F12 (3:1), 2% B27 without retinoic acid, 1% antibiotic-antimycotic
477 solution). For the first four media changes, RDM was supplemented with 10 µM SU5402 and 3 µM
478 CHIR99021.

479 After 60 days of differentiation, pigmented patches of RPE were micro-dissected, dissociated
480 using Trypsin-EDTA (0.25%), and plated on laminin coated surfaces in RDM with 10% FBS and Rho
481 kinase inhibitor (ROCKi; Y-27632). After 2 days, the media was changed to RDM with 2% FBS, and
482 eventually to RDM once the cells were fully confluent. There were no differences observed between RPE
483 differentiated from iPSCs cultured on MEFs and Matrigel. Mutant and wildtype genotypes of iPSC-RPE
484 were verified by Sanger sequencing periodically. Heparin (Cat# H-3149) and SU5402 (Cat# SML0443-

485 25MG) were from Sigma-Aldrich, CHIR99021 (Cat# 4423) was from Tocris Bioscience, and ReLeSR
486 was purchased from STEMCELL Technologies. All other differentiation reagents were purchased from
487 ThermoFisher Scientific.

488

489 **Gene expression analysis**

490 Reverse transcriptase-PCR was used to assess RPE-specific gene expression in RPE derived from
491 different iPSC lines as described previously (Singh et al., 2013b). Primers used are listed in **Table S2**.

492

493 **Generation of lentiviral (LV) vectors**

494 LV plasmid with the human *VMD2* promoter driving expression of *hBEST1-T2A-GFP* was
495 provided by Alfred S. Lewin (University of Florida). LentiCRISPR v2 (LCv2) plasmid was purchased
496 from Addgene (Cat# 52961), and molecular cloning was used to insert specific sgRNA sequences (**Table**
497 **S5**) as described (Steyer et al., 2018). LV plasmids for GE containing specific sgRNA sequences and the
498 human *VMD2* promoter driving expression of *spCas9-T2A-GFP* (**Table S3**) were then generated as
499 described hereafter (all primers used are listed in **Table S4**). To begin, the '*T2A-GFP-WPRE*' sequence
500 was amplified from the *hVMD2-hBEST1-T2A-GFP* plasmid using LCv2-GFP.Gib.F and .R primers and
501 Q5 2X MM (NEB, Cat# M0492L). The '*2A-Puro-WPRE*' sequence was then removed from the LCv2
502 plasmid via restriction digestion with PmeI (NEB, Cat# R0560S) and BamHI (NEB, Cat# R3136S). The
503 digestion product was resolved on a 0.7% agarose gel and the plasmid backbone was purified using the
504 Monarch gel purification kit (NEB, Cat# T1020S). The '*T2A-GFP-WPRE*' sequence was inserted into the
505 digested backbone using the Gibson Assembly kit (SGI, Cat# GA1100) per the manufacturer's
506 instructions. The completed Gibson Assembly reaction was then amplified using chemically competent *E.*
507 *coli* (NEB, Cat# C3040H) and Sanger sequenced to confirm insertion of '*T2A-GFP-WPRE*' using LCv2-

508 GFP.seq.L and LCv2-GFP.seq.R primers. This intermediate plasmid product (*pLCv2-GFP*) was digested
509 with AfeI (NEB, Cat# R0652S) and EcoRI-HF (NEB, Cat R310S) to remove the constitutive EF-1 alpha
510 core promoter. The desired digestion product was purified as described above. The *hVMD2* promoter was
511 then PCR amplified from *hVMD2-hBEST1-T2A-GFP* using Q5 2X MM and VMD2.LCv2.GFP.Gib.F and
512 .R primers, followed by insertion into the digested LCv2-GFP backbone via Gibson Assembly. Next, the
513 completed Gibson reaction was transformed into chemically competent *E. coli* and the sequence of the
514 final product *hVMD2-spCas9-T2A-GFP* was confirmed via Sanger sequencing using
515 VMD2.LCv2.GFP.seq.L and .R primers. Subsequently, specific sgRNAs were cloned into *hVMD2-*
516 *spCas9-T2A-GFP* using the same restriction digest and Gibson Assembly protocol described for
517 generation of the LCv2 GE vectors.

518

519 **LV production and cell transduction**

520 LV stocks were generated by the Cell Culture Core of the UW Department of Dermatology Skin
521 Disease Research Center (Madison, WI). Briefly, HEK293 cells cultured on 10-cm dishes were
522 transfected with LV plasmids—10 µg of sgRNA encoding LV plasmid (*hVMD2-hBEST1-T2A-GFP*,
523 *hVMD2-spCas9-T2A-GFP* or LCv2); 5 µg of psPax2 (Addgene, Cat# 12260), and 2 µg of pMD2.G
524 (Addgene, Cat# 12259)—using Lipofectamine (ThermoFisher; Cat# 11668019). After 15 hours, culture
525 medium (DMEM with 10% FBS) was replaced with fresh media containing 1% Penicillin-Streptomycin.
526 Media containing LV was collected the next day and viral titers (**Table S6**) were calculated using
527 QuickTiter Lentivirus Titer Kit (Cell Biolabs, Cat# VPK-107).

528 For iPSC transduction, iPSCs between passages 10-30 were cultured on Matrigel (Corning, Cat
529 #354230) coated plates in StemFlex (Gibco, Cat#A3349401) medium. Cells were then seeded at 15,000
530 cells/well on Matrigel-coated 48-well plates, and 48 hours post-seeding they were transduced with LV

531 containing LCv2 encoding *AAVSI*, R218C, or WT sgRNA at a dose of 0, 10, 100, or 500 μ l. StemFlex
532 medium was then added to a total volume of 750 μ l per well. 48 hours after LV treatment, the media was
533 replaced with 250 μ l of fresh StemFlex. At 96 hours after LV treatment, total genomic DNA was
534 harvested and analyzed via sequencing as described under the ‘Deep sequencing analysis of DNA and
535 RNA read frequency’ section.

536 For iPSC-RPE transduction, monolayers of iPSC-RPE on transwells were treated with 0, 5, 50, or
537 150 μ l (Figure 3e) or 150 μ l alone (GA experiments and Figures 3h, 3i) of specified LV preparation.
538 Media was changed on day 2 to RDM, and cells were maintained in culture with media changes every 3
539 days until used for sequencing or other analyses.

540

541 **Transepithelial electrical resistance (TER) measurements**

542 Monolayers of RPE cultured on transwell inserts (Corning, #3470) were used for all TER
543 measurements. To perform the measurements, we employed an epithelial voltohmmeter (EVOM2) with
544 chopstick electrodes (STX2) from World Precision Instruments (Sarasota, USA) according to
545 manufacturer’s instructions. Electrodes were sterilized with ethanol, and then rinsed in sterile Milli-Q
546 water followed by HBSS before measuring electrical resistance of RPE monolayers. Differences between
547 TER values of transwells with cultured RPE monolayers versus background measurements of cell-free
548 transwell inserts were multiplied by the surface area of the transwell membrane to obtain net TER values
549 in $\Omega \cdot \text{cm}^2$.

550

551 **CaCC current density measurements**

552 All iPSC-RPE cells used for chloride current measurements were cultured as a monolayer on
553 transwells. To singularize cells prior to measurement, transwells were washed twice with 0 Na-CMF

554 solution (135 mM N-Methyl-D-glucamine (NMDG)-Cl, 5 mM KCl, 10 mM HEPES, 10 mM glucose, 2
555 mM EDTA-KOH, pH adjusted to 7.4) and then incubated with papain enzyme solution (0 Na-CMF
556 solution containing 2.5 μ l/ml papain (46 mg/ml, MP Biomedicals LLC, Cat#100921), 0.375 mg/ml
557 adenosine, 0.3mg/ml L-cysteine, 0.25 mg/ml L- glutathione, and 0.05mg/ ml taurine) for 30 minutes at
558 37°C/5% CO₂. To stop the reaction, 0.01% BSA was added to the enzymatic solution. After washing
559 twice with 0 Na-CMF solution, cells were dispersed in extracellular solution containing 140 mM NaCl, 10
560 mM HEPES, 3 mM KCl, 2 mM CaCl₂, 2 mM MgCl₂, and 5.5 mM glucose adjusted to pH 7.4 with NaOH
561 by gentle pipetting.

562 Cells with polarized RPE morphology post-dissociation (**Figure 2b**, *left*) were used to measure
563 chloride currents. To test effects of GA or GE on *BEST1* mutant iPSC-RPE by single-cell patch clamp
564 analysis, only cells with GFP fluorescence (from transduction with *hVMD2-hBEST1-T2A-GFP* for GA or
565 *hVMD2-spCas9-T2A-GFP* encoding *AAVSI* sgRNA or MT allele-targeted sgRNAs for GE) were used.
566 Current recordings on these cells were performed using the conventional whole-cell patch clamp
567 technique with an Axopatch 200A amplifier controlled by Clampex software program via the digidata
568 1550 data acquisition system (Axon Instruments, CA). Fire-polished borosilicate glass pipettes with 3-5
569 M Ω resistance were filled with pipette solution containing 4.5 μ M calcium or no calcium.

570 Recordings were carried out at room temperature and current-voltage tracings were established
571 using ramps from -100 to +100 mV for 1000 ms. The pipette solution with calcium was comprised of (in
572 mM) 146 CsCl, 5 (Ca²⁺)-EGTA-NMDG, 2 MgCl₂, 8 HEPES, and 10 sucrose at pH 7.3, adjusted with
573 NMDG. Another pipette solution devoid of calcium was comprised of (in mM) 146 CsCl, 5 EGTA-
574 NMDG, 2 MgCl₂, 8 HEPES, and 10 Sucrose at pH 7.3, adjusted with NMDG. Both of these pipette
575 solutions were mixed to make the solution containing 4.5 μ M free calcium as described
576 previously(Kuruma and Hartzell, 2000), which was then used for patch clamping.

577 Current density values were obtained by dividing current amplitude with cell capacitance
578 measurements. CaCC current densities for iPSC-RPE are represented as differences between mean 4.5
579 μ M calcium response and mean no calcium response from a total of at least five cells for each condition.
580 At least two differentiations were used as replicates to obtain data for each line.

581

582 **Immunocytochemistry**

583 iPSC-RPE cultured on transwell inserts were washed with PBS and fixed with 4%
584 paraformaldehyde for 10 minutes at room temperature (RT). After washing fixed cells three times with
585 PBS, transwell membranes were placed in blocking solution (10% normal donkey serum with 5% BSA,
586 1% fish gelatin and 0.5% Triton-X100 in PBS) for one hour at RT, and then incubated overnight at 4 °C
587 in primary antibody (1:100 mouse anti-Bestrophin (Millipore, Cat# MAB5466); 1:100 rabbit anti-ZO-1
588 (ThermoFisher Scientific, Cat# 61-7300)) prepared in blocking solution. Cells were then washed three
589 times in PBS and incubated for 30 minutes at RT in appropriate secondary antibody (ThermoFisher
590 Scientific; 1:500 Donkey anti-Mouse IgG (Cat# A31571); 1:500 Donkey anti-Rabbit IgG (Cat# A10040))
591 prepared in blocking solution. Cells were again washed three times in PBS, incubated in DAPI (1:500;
592 ThermoFisher; Cat# D1306) for 30 minutes, mounted using prolong gold with DAPI (ThermoFisher; Cat#
593 P36931), and imaged using Nikon A1R confocal microscope with NIS Elements AR 5.0 software.

594

595 **Photoreceptor outer segment (POS) phagocytosis and rhodopsin degradation assay**

596 POS feeding of iPSC-RPE was performed as described previously (Singh et al., 2013b). Briefly, bovine
597 POS (InVision BioResources (Seattle, WA)) were gently resuspended in DMEM. 100 μ l media was then
598 removed from each transwell insert, 6.25×10^6 POS were added, and cells were incubated at 37 °C and 5%
599 CO₂ for 2 hours. Afterward, POS containing RDM was removed and each transwell was washed

600 thoroughly three times using DPBS. Following the washes, cells were harvested (0 time point) or further
601 incubated in fresh RDM for prescribed periods of time. At each time point, transwells were washed, 100
602 μ l RIPA buffer (ThermoFisher; Cat# 89900) containing protease inhibitor cocktail (Sigma-Aldrich; Cat#
603 P8340) was added, and cells were incubated on ice for 30 minutes to extract total cell protein. Protein
604 quantification was performed using the DC Protein assay kit II (Bio-Rad, Cat# 5000112).

605 Western blots were then performed to monitor rhodopsin degradation as described (Singh et al.,
606 2015; Singh et al., 2013b). Briefly, protein lysates were denatured in 1X Laemmli buffer (reducing) and
607 kept on ice for 10 minutes. Protein samples were then separated on 4-20% mini-Protean TGX gels (Bio-
608 Rad; Cat# 4568095) and electroblotted onto PVDF membranes (Millipore; IPFL10100). After blotting,
609 membranes were dried at RT for 15 minutes, re-activated in methanol for 1 minute, and then incubated in
610 blocking buffer (1:1 Odyssey blocking buffer (LI-COR Biosciences; Cat# 927-40000):PBS) for 1 hour.
611 Post-blocking, blots were incubated in primary antibodies (1:500 mouse anti-rhodopsin (Millipore, Cat#
612 MABN15); 0.1 μ g/ml rabbit anti-beta actin (Abcam, Cat# ab8227)) in blocking buffer with 0.1% Tween-
613 20 overnight, washed three times for 5 minutes each in PBS with 0.1% Tween-20, incubated for 1.5 hours
614 at RT in appropriate secondary antibody (LI-COR Biosciences; 1:20,000 Donkey anti-Rabbit IgG (Cat#
615 926-32213); 1:20,000 Donkey anti-Mouse IgG (Cat# 926-68022)) in blocking buffer with 0.1% Tween-
616 20 and 0.01% SDS, and then washed three times for 5 minutes each in PBS with 0.1% Tween-20. An
617 Odyssey infrared Imager (LI-COR Biosciences) was used to image blots using Image Studio software.
618 ImageJ was used for quantification of relevant protein bands.

619

620 **Deep sequencing analysis of DNA and RNA read frequency**

621 Cells were singularized with TrypLE Express (Gibco, Cat# 12605010) per manufacturer's
622 instructions. Total DNA and/or RNA was extracted using QuickExtract DNA (Epicentre, Cat# QE09050)

623 or QuickExtract RNA (Epicentre, Cat# QER090150), respectively. Both DNA and RNA extractions were
624 performed per manufacturer's instructions with the following minor modifications: 1) a ratio of 10,000-
625 25,000 cells per 50 μ l of QuickExtract solution was routinely used, and 2) an optional DNase 1 treatment
626 was omitted from the RNA extraction protocol. All samples were stored at -80 °C until use.
627 RNA was reverse transcribed to cDNA using the ProtoScript II First Strand synthesis kit (NEB, Cat#
628 E6560S) and synthesis was performed with the "random primer" option included within the kit. 4 μ l of
629 crude RNA extract was added to each cDNA reaction.

630 In preparation for targeted deep sequencing, Illumina adapter sequences and sample-specific
631 barcodes were appended to genomic or cDNA amplicons via overhang PCR as described(Steyer et al.,
632 2018).
633 Purified amplicon libraries were assembled into 2 nM total DNA in DNase/RNase free H₂O and
634 sequenced using 150 nucleotide paired end reads using MiSeq (6M or 15M total reads) at the UW Biotech
635 Center (Madison, WI) with the following loading condition: 8 pmol total DNA and 15% PhiX DNA.
636 Raw FASTQ files were read and aligned to expected amplicons using a command line implementation of
637 CRISPResso (v1.0.8)(Pinello et al., 2016). Full commands used for analysis are provided in the Source
638 Data for each corresponding Supplemental Figure panel. 'Percent allele identity' or 'percent edited' were
639 determined using the software's standard output table of individual read identities. Sequencing reads with
640 counts <100 were not included in the analysis. All FASTQ files are available upon request.

641

642 **Single-cell RNA sequencing (scRNA-seq)**

643 iPSC-RPE cultures from the A146K, N296H, and R218C adBD patient lines and an isogenic
644 gene-corrected control line derived from the R218C line (R218C>WT) were transduced with 150 μ l of
645 *hVMD2-spCas9-T2A-GFP* encoding specific sgRNAs as described in the 'LV production and cell

646 transduction' section. For each sample, sgRNAs were either targeted to mutant *BEST1* or to the *AAVSI*
647 locus (control). On day 14, cells were dissociated from transwells with a papain dissociation kit
648 (Worthington Biochemical, Cat# LK003150) and filtered using a Flowmi cell strainer (Bel-Art SP
649 Scienceware, Cat# H13680-0040) to obtain single-cell suspension. Cells were then prepared for scRNA-
650 seq with the droplet-based 10X Genomics GemCode platform according to the manufacturer's
651 instructions. In brief, singularized cells were encapsulated in oil beads containing a unique molecular
652 identifier (UMI) barcode. The cells were then lysed and cDNA libraries were created featuring cell and
653 transcript-specific molecular identifiers. Libraries were sequenced using an Illumina HiSeq2500 Rapid
654 Run and reads were aligned to a custom reference genome consisting of the human hg19 GRCh38
655 genome and an added gene for the *spCas9-T2A-GFP* transcript.

656

657 **scRNA-seq data analysis**

658 Genome edited iPSC-RPE were clustered based on their genome-wide transcriptome using the t-
659 Distributed Stochastic Neighbor Embedding (t-SNE) algorithm with the 10X Genomics Loupe Cell
660 Browser software (v2.0.0). Reads for each pair of samples (*BEST1* mutant allele-targeted sgRNA vs
661 *AAVSI* sgRNA control) were aligned, analyzed, clustered with Cell Ranger v2.1.1, and compared to
662 detect significant differences in gene expression, with p values adjusted using the Benjamini-Hochberg
663 correction for multiple tests. $P < 0.01$ was used as the significance threshold for all analyses. Cell Ranger
664 using the aggregate feature was run to concatenate each pair of samples with the same genotype, and
665 differential gene expression within each pair (with gene editing at either the *AAVSI* or *BEST1* locus) was then
666 analyzed. Potential adverse events were probed using gene lists curated from gene ontology terms
667 associated with the cell cycle, apoptosis, DNA damage response, and the innate immune response, as well
668 as a list of 149 validated marker genes associated with human RPE (Strunnikova et al., 2010)

669 **(Supplemental Data File C**; gene ontology sets are available on the Molecular Signatures Database
670 <http://software.broadinstitute.org/gsea/msigdb>). Differentially-expressed genes with $p < 0.01$ were
671 deemed to be significant. All significantly differentially-expressed genes per cluster are reported, with the
672 exception of genes identified by Cell Ranger as having low average UMI counts. Volcano plots were generated
673 in RStudio (v.1.1.456) using the ggplot2 package.

674

675 **Non-negative matrix factorization-based comparison of scRNA-seq datasets**

676 Non-negative matrix factorization (NMF) followed by clustering of genes using the NMF factors was
677 used for **Figure S7B** to project each dataset into a gene group. The input data for this analysis were a set of
678 gene barcode matrices generated using the Cell Ranger 2.1.1 algorithm. The matrices were filtered to remove
679 background barcodes in order to include only detected cellular barcodes, and then further filtered to exclude
680 cells expressing fewer than 2000 total counts, followed by depth normalization.

681 To enable comparison of transcriptional signatures from each sample, NMF(Lee and Seung, 2000)
682 was applied to each scRNA-seq dataset. NMF is a popular dimensionality reduction and clustering
683 approach that is used to project data into low dimensional non-negative factors, and thus can be used to
684 derive a clustering of cells and genes. NMF with $k=10$ factors was applied with a total of five NMF runs.
685 Next, the similarity of NMF results was compared between two samples using the average best Jaccard
686 coefficient between clusters of one versus another sample. 1-average Jaccard coefficient was then used as
687 the distance to apply hierarchical clustering on the samples. This procedure was repeated five times and
688 the tree that appeared most often was used. The trees learned in different iterations were largely similar
689 and always grouped the patient-specific lines first before grouping different lines together.

690

691 **QUANTIFICATION AND STATISTICAL ANALYSIS**

692 Unless otherwise specified, all analyses were performed using GraphPad Prism (v.8.0.1) and error
693 bars represent mean \pm SD; ns = $p \geq 0.05$, * for $p < 0.05$, ** for $p < 0.01$, *** for $p < 0.001$, **** for p
694 < 0.0001 . Further detail for each analysis is provided here. Statistical analyses for Figures 2i and 3k were
695 performed using Origin 2018b. Student's *t*-test was performed to measure the significance between the
696 groups. P values < 0.05 were considered statistically significant. Statistical significance for Figure 3h and 3i
697 was determined using the Holm-Sidak method with $\alpha = 0.05$. Each row was analyzed individually, without
698 assuming a consistent SD (number of *t* tests = 10 and 2 for Figure 3h, and 3i, respectively). Statistical
699 significance for differential gene expression in Figures 3n and Figure S7c was determined using the Cell
700 Ranger 2.1.1 algorithm. Sample pairs with each genotype were analyzed and clustered with individual Cell
701 Ranger runs for each pair and analyzed using the Loupe Cell Browser (v.2.0.0). Differential expression was
702 calculated using a negative binomial exact test, and p values were adjusted using the Benjamini-Hochberg
703 correction for multiple tests. $P < 0.01$ was used as the threshold for assigning significant versus non-
704 significant changes in gene expression. Volcano plots were generated in RStudio (v 1.1.456) using the
705 ggplot2 package. For Figures S5B and S5C, discovery was determined using the two-stage linear step-up
706 procedure of Benjamini, Krieger, and Yekutieli with $Q = 1\%$. Each row was analyzed individually, without
707 assuming a consistent SD (number of *t* tests = 3).

708

709 **DATA AND SOFTWARE AVAILABILITY**

710 Upon acceptance, scRNA-seq data will be posted to an accession database. Raw targeted
711 sequencing files for DNA and RNA sequencing data will be deposited to the NCBI Trace and Short-Read
712 Archive. Raw patch clamp data are available upon request. All other experimental data are provided in the
713 source data files or in Supplemental data.

714

715 **REFERENCES**

- 716 Bakondi, B., Lv, W.J., Lui, B., Jones, M.K., Tsai, Y., Kim, K.J., Levy, R., Akhtar, A.A., Breunig, J.J.,
717 Svendseni, C.N., *et al.* (2016). In Vivo CRISPR/Cas9 Gene Editing Corrects Retinal Dystrophy in the
718 S334ter-3 Rat Model of Autosomal Dominant Retinitis Pigmentosa. *Mol Ther* 24, 556-563.
- 719
- 720 Boon, C.J.F., Klevering, B.J., Leroy, B.P., Hoyng, C.B., Keunen, J.E.E., and den Hollander, A.I. (2009).
721 The spectrum of ocular phenotypes caused by mutations in the BEST1 gene. *Prog Retin Eye Res* 28, 187-
722 205.
- 723
- 724 Courtney, D.G., Moore, J.E., Atkinson, S.D., Maurizi, E., Allen, E.H., Pedrioli, D.M., McLean, W.H.,
725 Nesbit, M.A., and Moore, C.B. (2016). CRISPR/Cas9 DNA cleavage at SNP-derived PAM enables both
726 in vitro and in vivo KRT12 mutation-specific targeting. *Gene Ther* 23, 108-112.
- 727
- 728 Cox, D.B., Platt, R.J., and Zhang, F. (2015). Therapeutic genome editing: prospects and challenges. *Nat*
729 *Med* 21, 121-131.
- 730
- 731 Cromer, M.K., Vaidyanathan, S., Ryan, D.E., Curry, B., Lucas, A.B., Camarena, J., Kaushik, M., Hay,
732 S.R., Martin, R.M., Steinfeld, I., *et al.* (2018). Global Transcriptional Response to CRISPR/Cas9-AAV6-
733 Based Genome Editing in CD34(+) Hematopoietic Stem and Progenitor Cells. *Mol Ther* 26, 2431-2442.
- 734
- 735 Cukras, C., Wiley, H.E., Jeffrey, B.G., Sen, H.N., Turriff, A., Zeng, Y., Vijayasarathy, C., Marangoni, D.,
736 Ziccardi, L., Kjellstrom, S., *et al.* (2018). Retinal AAV8-RS1 Gene Therapy for X-Linked Retinoschisis:
737 Initial Findings from a Phase I/IIa Trial by Intravitreal Delivery. *Mol Ther* 26, 2282-2294.

738

739 Dickson, V.K., Pedi, L., and Long, S.B. (2014). Structure and insights into the function of a Ca²⁺-
740 activated Cl⁻ channel. *Nature* 516, 213-218.

741

742 Doudna, J.A., and Charpentier, E. (2014). The new frontier of genome engineering with CRISPR-Cas9.
743 *Science* 346, 1077-+.

744

745 George, A.L., Jr. (2004). Inherited Channelopathies Associated with Epilepsy. *Epilepsy Curr* 4, 65-70.

746

747 Guziewicz, K.E., Cideciyan, A.V., Beltran, W.A., Komaromy, A.M., Dufour, V.L., Swider, M., Iwabe, S.,
748 Sumaroka, A., Kendrick, B.T., Ruthel, G., *et al.* (2018). BEST1 gene therapy corrects a diffuse retina-
749 wide microdetachment modulated by light exposure. *P Natl Acad Sci USA* 115, E2839-E2848.

750

751 Guziewicz, K.E., Sinha, D., Gomez, N.M., Zorych, K., Dutrow, E.V., Dhingra, A., Mullins, R.F., Stone,
752 E.M., Gamm, D.M., Boesze-Battaglia, K., *et al.* (2017). Bestrophinopathy: An RPE-photoreceptor
753 interface disease. *Prog Retin Eye Res* 58, 70-88.

754

755 Johnson, A.A., Guziewicz, K.E., Lee, C.J., Kalathur, R.C., Pulido, J.S., Marmorstein, L.Y., and
756 Marmorstein, A.D. (2017). Bestrophin 1 and retinal disease. *Prog Retin Eye Res* 58, 45-69.

757

758 Kuruma, A., and Hartzell, H.C. (2000). Bimodal control of a Ca⁽²⁺⁾-activated Cl⁽⁻⁾ channel by different
759 Ca⁽²⁺⁾ signals. *J Gen Physiol* 115, 59-80.

760

761 Kuscu, C., Arslan, S., Singh, R., Thorpe, J., and Adli, M. (2014). Genome-wide analysis reveals
762 characteristics of off-target sites bound by the Cas9 endonuclease. *Nat Biotechnol* 32, 677-683.

763 Lam, B.L., Davis, J.L., Gregori, N.Z., MacLaren, R.E., Girach, A., Verriotto, J.D., Rodriguez, B., Rosa,
764 P.R., Zhang, X., and Feuer, W.J. (2019). Choroideremia Gene Therapy Phase 2 Clinical Trial: 24-Month
765 Results. *Am J Ophthalmol* 197, 65-73.

766

767 Ledford, H. (2017). FDA advisers back gene therapy for rare form of blindness. *Nature* 550, 314.

768

769 Lee, D.D., and Seung, H.S. (2000). Algorithms for Non-negative Matrix Factorization. *Advances in*
770 *Neural Information Processing Systems* 13, 556-562.

771

772 Li, P., Kleinstiver, B.P., Leon, M.Y., Prew, M.S., Navarro-Gomez, D., Greenwald, S.H., Pierce, E.A.,
773 Joung, J.K., Liu, Q. (2018). Allele-Specific CRISPR-Cas9 Genome Editing of the Single-Base P23H
774 Mutation for Rhodopsin-Associated Dominant Retinitis Pigmentosa. *The CRISPR Journal* 1, 55-64.

775

776 Li, Y., Zhang, Y., Xu, Y., Kittredge, A., Ward, N., Chen, S., Tsang, S.H., and Yang, T. (2017). Patient-
777 specific mutations impair BESTROPHIN1's essential role in mediating Ca(2+)-dependent Cl(-) currents
778 in human RPE. *Elife* 6.

779

780 Mali, P., Yang, L., Esvelt, K.M., Aach, J., Guell, M., DiCarlo, J.E., Norville, J.E., and Church, G.M.
781 (2013). RNA-guided human genome engineering via Cas9. *Science* 339, 823-826.

782

- 783 Milenkovic, A., Milenkovic, V.M., Wetzel, C.H., and Weber, B.H.F. (2018). BEST1 protein stability and
784 degradation pathways differ between autosomal dominant Best disease and autosomal recessive
785 bestrophinopathy accounting for the distinct retinal phenotypes. *Hum Mol Genet* 27, 1630-1641.
786
- 787 Pattanayak, V., Lin, S., Guilinger, J.P., Ma, E., Doudna, J.A., and Liu, D.R. (2013). High-throughput
788 profiling of off-target DNA cleavage reveals RNA-programmed Cas9 nuclease specificity. *Nat Biotechnol*
789 31, 839-843.
790
- 791 Pawan K. Shahi, D.H., Divya Sinha, Simran Brar, Hannah Moulton, Sabrina Stulo, Katarzyna D. Borys,
792 Elizabeth Capowski, De-Ann M. Pillers, David M. Gamm, Bikash R. Pattnaik (2019). Gene augmentation
793 and read-through rescue channelopathy in an iPSC-RPE model of congenital blindness. *American Journal*
794 *of Human Genetics*.
795
- 796 Pinello, L., Canver, M.C., Hoban, M.D., Orkin, S.H., Kohn, D.B., Bauer, D.E., and Yuan, G.C. (2016).
797 Analyzing CRISPR genome-editing experiments with CRISPResso. *Nat Biotechnol* 34, 695-697.
798
- 799 Popp, M.W., and Maquat, L.E. (2016). Leveraging Rules of Nonsense-Mediated mRNA Decay for
800 Genome Engineering and Personalized Medicine. *Cell* 165, 1319-1322.
801
- 802 Russell, S., Bennett, J., Wellman, J.A., Chung, D.C., Yu, Z.F., Tillman, A., Wittes, J., Pappas, J., Elci, O.,
803 McCague, S., *et al.* (2017). Efficacy and safety of voretigene neparvovec (AAV2-hRPE65v2) in patients
804 with RPE65-mediated inherited retinal dystrophy: a randomised, controlled, open-label, phase 3 trial.
805 *Lancet* 390, 849-860.

806

807 Sadelain, M., Papapetrou, E.P., and Bushman, F.D. (2011). Safe harbours for the integration of new DNA
808 in the human genome. *Nat Rev Cancer* 12, 51-58.

809

810 Schaaf, C.P. (2014). Nicotinic acetylcholine receptors in human genetic disease. *Genet Med* 16, 649-656.

811

812 Shen, M.W., Arbab, M., Hsu, J.Y., Worstell, D., Culbertson, S.J., Krabbe, O., Cassa, C.A., Liu, D.R.,

813 Gifford, D.K., and Sherwood, R.I. (2018). Predictable and precise template-free CRISPR editing of

814 pathogenic variants. *Nature* 563, 646-651.

815 Singh, R., Kuai, D., Guziewicz, K.E., Meyer, J., Wilson, M., Lu, J., Smith, M., Clark, E., Verhoeven, A.,

816 Aguirre, G.D., *et al.* (2015). Pharmacological Modulation of Photoreceptor Outer Segment Degradation in

817 a Human iPS Cell Model of Inherited Macular Degeneration. *Mol Ther* 23, 1700-1711.

818

819 Singh, R., Phillips, M.J., Kuai, D., Meyer, J., Martin, J.M., Smith, M.A., Perez, E.T., Shen, W., Wallace,

820 K.A., Capowski, E.E., *et al.* (2013a). Functional analysis of serially expanded human iPS cell-derived

821 RPE cultures. *Invest Ophthalmol Vis Sci* 54, 6767-6778.

822

823 Singh, R., Shen, W., Kuai, D., Martin, J.M., Guo, X.R., Smith, M.A., Perez, E.T., Phillips, M.J.,

824 Simonett, J.M., Wallace, K.A., *et al.* (2013b). iPS cell modeling of Best disease: insights into the

825 pathophysiology of an inherited macular degeneration. *Hum Mol Genet* 22, 593-607.

826

827 Steyer, B., Bu, Q., Cory, E., Jiang, K., Duong, S., Sinha, D., Steltzer, S., Gamm, D., Chang, Q., and Saha,
828 K. (2018). Scarless Genome Editing of Human Pluripotent Stem Cells via Transient Puromycin Selection.
829 *Stem Cell Reports* *10*, 642-654.

830

831 Strunnikova, N.V., Maminishkis, A., Barb, J.J., Wang, F., Zhi, C., Sergeev, Y., Chen, W., Edwards, A.O.,
832 Stambolian, D., Abecasis, G., *et al.* (2010). Transcriptome analysis and molecular signature of human
833 retinal pigment epithelium. *Hum Mol Genet* *19*, 2468-2486.

834

835 Tsai, Y.T., Wu, W.H., Lee, T.T., Wu, W.P., Xu, C.L., Park, K.S., Cui, X., Justus, S., Lin, C.S., Jauregui,
836 R., *et al.* (2018). Clustered Regularly Interspaced Short Palindromic Repeats-Based Genome Surgery for
837 the Treatment of Autosomal Dominant Retinitis Pigmentosa. *Ophthalmology* *125*, 1421-1430.

838

839 Vasireddy, V., Mills, J.A., Gaddameedi, R., Basner-Tschakarjan, E., Kohnke, M., Black, A.D.,
840 Alexandrov, K., Zhou, S., Maguire, A.M., Chung, D.C., *et al.* (2013). AAV-mediated gene therapy for
841 choroideremia: preclinical studies in personalized models. *PLoS One* *8*, e61396.

842

843 Villa, C., and Combi, R. (2016). Potassium Channels and Human Epileptic Phenotypes: An Updated
844 Overview. *Front Cell Neurosci* *10*, 81.

845

846 Waugh, N., Loveman, E., Colquitt, J., Royle, P., Yeong, J.L., Hoad, G., and Lois, N. (2018). Treatments
847 for dry age-related macular degeneration and Stargardt disease: a systematic review. *Health Technol*
848 *Assess* *22*, 1-168.

849

850 Wienert, B., Shin, J., Zelin, E., Pestal, K., and Corn, J.E. (2018). In vitro-transcribed guide RNAs trigger
851 an innate immune response via the RIG-I pathway. *PLoS Biol* 16, e2005840.

852

853 Yang, T., Liu, Q., Kloss, B., Bruni, R., Kalathur, R.C., Guo, Y., Kloppmann, E., Rost, B., Colecraft,
854 H.M., and Hendrickson, W.A. (2014). Structure and selectivity in bestrophin ion channels. *Science* 346,
855 355-359.

856

857 **SUPPLEMENTAL DATA**

858

859 **Data Figures (attached below):**

860 Data S1. R141H/A195V ARB iPSC line characterization.

861 Data S2. Western blots for rhodopsin degradation assays.

862

863 **Supplemental Tables (attached below):**

864 Table S1. List of iPSC lines used and their subsequent characterization.

865 Table S2: RPE-specific RT-PCR primers used.

866 Table S3. List of GE vectors used.

867 Table S4. List of primers for lentiviral plasmid generation.

868 Table S5. List of sgRNAs.

869 Table S6. Lentivirus titers.

870 Table S7. Primers for deep sequencing of DNA and cDNA.

871 Table S8. Number of cells used for CaCC current density measurements.

872

873 **Supplemental Data Files (available for download):**

874 Supplemental Data File A. Replicates for frameshift analysis of iPSC+GE versus iPSC-RPE+GE.

875 Supplemental Data File B. Comparison of experimental indel frequency outcomes in iPSC-RPE+GE

876 versus outcomes predicted by the inDelphi tool.

877 Supplemental Data File C. Curated gene sets used to assess differences in gene expression between

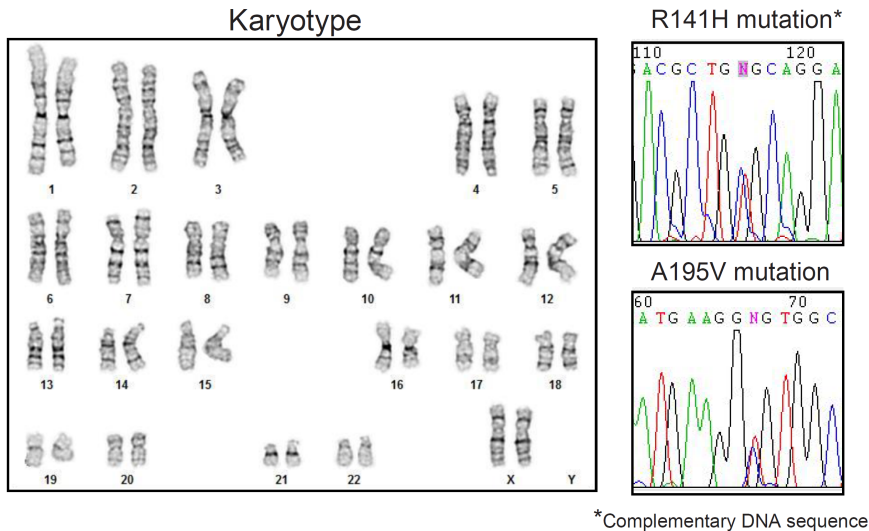
878 control (*AAVSI*) and MT *BEST1* allele-targeted sgRNA in Figure S7C.

879 Supplemental Data File D. Ranked off-target sites for sgRNAs used in this study.

880

881 DATA FIGURES

882 Data S1. R141H/A195V ARB iPSC line characterization.



Pluripotency analysis

| Self-renewal | | |
|--------------|-------------|-------------|
| Gene | P10 | P22 |
| CXCL5 | 3.78 | 3.34 |
| DNMT3B | 0.12 | 0.13 |
| HESX1 | 0.14 | 0.17 |
| IDO1 | 1.23 | 1.38 |
| LCK | 0.84 | 0.60 |
| NANOG | 1.60 | 1.43 |
| POU5F1 | 0.30 | 0.27 |
| SOX2 | 1.09 | 1.12 |
| TRIM22 | 2.64 | 2.36 |
| Average | 1.30 | 1.20 |

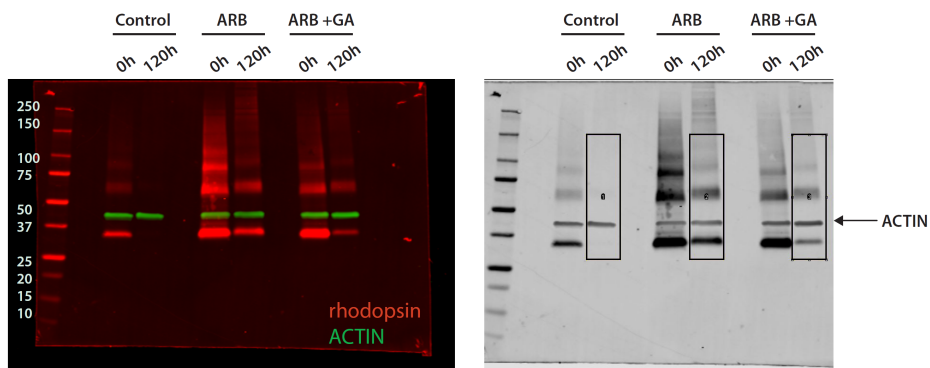
| Fold change legend | |
|--------------------|----------------------|
| fc > 100 | Upregulated |
| 10 < fc ≤ 100 | |
| 2 < fc ≤ 10 | |
| 0.5 ≤ fc ≤ 2 | Comparable |
| 0.1 ≤ fc < 0.5 | |
| 0.01 ≤ fc < 0.1 | |
| fc < 0.01 | Downregulated |

| Ectoderm markers | | | Mesoderm markers | | | Endoderm markers | | |
|----------------------|-------|-------|------------------|------|------|------------------|------|------|
| Target Name | P10 | P22 | Target Name | P10 | P22 | Target Name | P10 | P22 |
| CDH9 | 1.52 | 2.13 | ABCA4 | 1.11 | 1.29 | AFP | 0.00 | 0.00 |
| COL2A1 | 3.07 | 2.73 | ALOX15 | 0.20 | 0.21 | CABP7 | 0.14 | 0.24 |
| DMBX1 | 2.13 | 3.03 | BMP10 | 0.03 | 0.02 | CDH20 | 0.12 | 0.16 |
| DRD4 | 0.14 | 0.22 | CDH5 | 0.35 | 0.27 | CLDN1 | 0.50 | 0.46 |
| EN1 | 0.20 | 0.23 | CDX2 | 0.07 | 0.05 | CPLX2 | 0.07 | 0.05 |
| LMX1A | 0.07 | 0.20 | COLEC10 | 1.33 | 1.50 | ELAVL3 | 0.38 | 0.48 |
| MAP2 | 1.41 | 0.97 | ESM1 | 0.01 | 0.01 | EOMES | 0.02 | 0.02 |
| MYO3B | 0.97 | 0.81 | FCN3 | 0.62 | 0.48 | FOXA1 | 0.00 | 0.00 |
| NOS2 | 0.31 | 0.31 | FOXF1 | 0.27 | 0.27 | FOXA2 | 0.00 | 0.00 |
| NR2F1/NR2F2 | 0.00 | 0.00 | HAND1 | 0.01 | 0.01 | FOXP2 | 0.41 | 0.34 |
| NR2F2 | 0.04 | 0.12 | HAND2 | 0.09 | 0.25 | GATA4 | 0.02 | 0.01 |
| OLFM3 | 0.16 | 0.15 | HEY1 | 1.39 | 0.79 | GATA6 | 0.00 | 0.01 |
| PAPLN | 1.07 | 0.92 | HOPX | 0.31 | 3.27 | HHEX | 0.23 | 0.25 |
| PAX3 | 0.02 | 0.02 | IL6ST | 0.81 | 0.65 | HMP19 | 0.27 | 0.37 |
| PAX6 | 0.02 | 0.05 | NKX2-5 | 0.16 | 0.18 | HNF1B | 0.04 | 0.02 |
| POU4F1 | 0.04 | 0.19 | ODAM | 0.02 | 0.02 | HNF4A | 0.01 | 0.00 |
| PRKCA | 0.30 | 0.36 | PDGFRA | 0.16 | 0.14 | KLF5 | 0.49 | 0.51 |
| SDC2 | 9.64 | 8.17 | PLVAP | 0.41 | 0.36 | LEFTY1 | 0.04 | 0.01 |
| SOX1 | 0.10 | 0.05 | RGS4 | 0.10 | 0.09 | LEFTY2 | 0.05 | 0.03 |
| TRPM8 | 0.45 | 0.35 | SNAI2 | 0.18 | 0.25 | NODAL | 0.07 | 0.05 |
| WNT1 | 0.71 | 0.92 | TBX3 | 0.01 | 0.01 | PHOX2B | 0.01 | 0.01 |
| ZBTB16 | 0.13 | 0.08 | TM4SF1 | 0.08 | 0.06 | POU3F3 | 0.02 | 0.00 |
| | | | CXCL5 | 3.78 | 3.34 | PRDM1 | 0.16 | 0.20 |
| | | | DNMT3B | 0.12 | 0.13 | RXRG | 0.09 | 0.07 |
| | | | HESX1 | 0.14 | 0.17 | SOX17 | 0.00 | 0.00 |
| | | | IDO1 | 1.23 | 1.38 | SST | 0.16 | 0.10 |
| | | | LCK | 0.84 | 0.60 | | | |
| | | | NANOG | 1.60 | 1.43 | | | |
| | | | POU5F1 | 0.30 | 0.27 | | | |
| | | | SOX2 | 1.09 | 1.12 | | | |
| | | | TRIM22 | 2.64 | 2.36 | | | |
| | | | | | | | | |
| Mesoendoderm markers | | | | | | | | |
| Target Name | P10 | P22 | | | | | | |
| FGF4 | 0.29 | 0.25 | | | | | | |
| GDF3 | 1.26 | 0.87 | | | | | | |
| NPPB | 0.00 | 0.00 | | | | | | |
| NR5A2 | 44.39 | 34.18 | | | | | | |
| PTHLH | 0.29 | 0.38 | | | | | | |
| T | 0.00 | 0.00 | | | | | | |

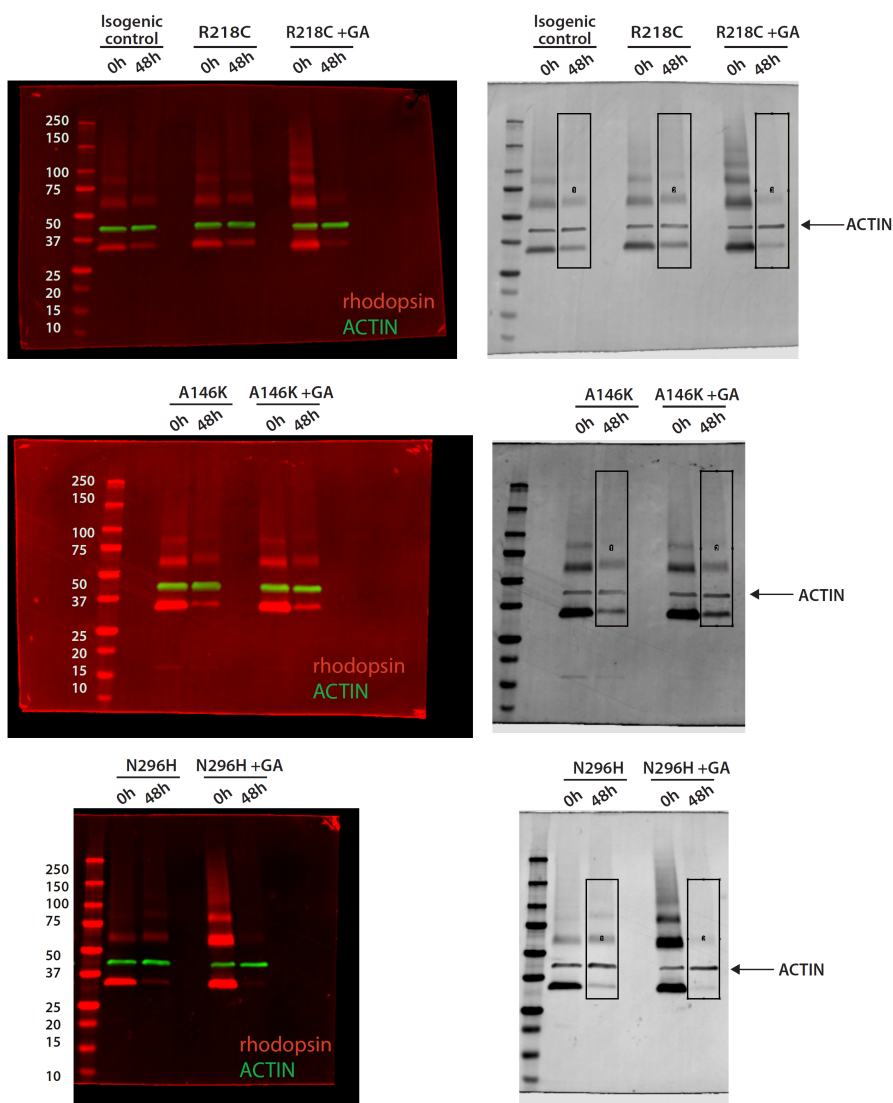
884 Data S2. Western blots for rhodopsin degradation assays.

Blots used for POS degradation graphs in Figure 2e (boxes represent areas used for quantification).

Boxed area was selected to include bands corresponding to fully denatured rhodopsin and its aggregated forms.



Blots used for POS degradation graphs in Figure 2h (boxes represent areas used for quantification).



885

886 **SUPPLEMENTAL TABLES**

887 **Table S1. List of iPSC lines used and their subsequent characterization.**

| iPSC line | <i>BEST1</i> Genotype | Karyotype | Pluripotency Confirmation | Reference |
|---------------------------------|--|------------------|----------------------------------|--|
| Normal | WT/WT | Yes | Yes | Singh et al., Hum Mol Genet., 2013 |
| R218C>WT Isogenic Control | WT/WT (isogenic to R218C/WT adBD iPSC line) | Yes | Yes | Steyer et al., Stem Cell Reports, 2018 |
| R218C adBD | R218C/WT | Yes | Yes | Steyer et al., Stem Cell Reports, 2018 |
| N296H adBD | N296H/WT | Yes | Yes | Singh et al., Hum Mol Genet., 2013 |
| A146K adBD | A146K/WT | Yes | Yes | Singh et al., Hum Mol Genet., 2013 |
| R141H/A195V ARB | R141H/A195V | Yes | Yes | Data S1 |

888

889

890 **Table S2: RPE-specific RT-PCR primers used.**

891

| <i>Gene</i> | Forward Primer | Reverse Primer |
|-----------------|--------------------------|------------------------------|
| <i>BEST1</i> | ATTTATAGGCTGGCCCTCACGGAA | TGTTCTGCCGGAGTCATAAAGCCT |
| <i>MITF</i> | TTCACGAGCGTCCTGTATGCAGAT | TTGCAAAGCAGGATCCATCAAGCC |
| <i>PEDF</i> | AATCCATCATTACCGGGCTCTCT | TGCACCCAGTTGTTGATCTCTTGC |
| <i>RPE65</i> | GCCCTCCTGCACAAGTTTGACTTT | AGTTGGTCTCTGTGCAAGCGTAGT |
| <i>OCCLUDIN</i> | TCATTGCCGCGTTGGTGATCTTTG | ATGATGCCCAGGATAGCACTCACT |
| <i>CRALBP</i> | TTCCGCATGGTACCTGAAGAGGAA | ACTGCAGCCGGAAATTCACATAGC |
| <i>GAPDH</i> | CAACGGATTTGGTCGTATTGG | GCAACAATATCCACTTTACCACAGTTAA |

892

893

894 **Table S3. List of GE vectors used.**

895

| GE Vector Name | sgRNA Name | Vector Backbone | Backbone Source |
|-----------------------|-------------------|-----------------------------|--------------------------------------|
| LCv2. <i>AAVSI</i> | <i>AAVSI</i> | LentiCRISPRv2 | Sanjana et al, Nat Methods, 2014 |
| LCv2.R218C | R218C | LentiCRISPRv2 | Sanjana et al, Nat Methods, 2014 |
| LCv2.WT | WT | LentiCRISPRv2 | Sanjana et al, Nat Methods. 2014 |
| VMD2. <i>AAVSI</i> | <i>AAVSI</i> | <i>hVMD2-spCas9-T2A-GFP</i> | Alfred Lewin (University of Florida) |
| VMD2.R218C | R218C | <i>hVMD2-spCas9-T2A-GFP</i> | Alfred Lewin (University of Florida) |
| VMD2.WT | WT | <i>hVMD2-spCas9-T2A-GFP</i> | Alfred Lewin (University of Florida) |
| VMD2.N296H | N296H | <i>hVMD2-spCas9-T2A-GFP</i> | Alfred Lewin (University of Florida) |
| VMD2.A146K | A146K | <i>hVMD2-spCas9-T2A-GFP</i> | Alfred Lewin (University of Florida) |

896

897

898
899

Table S4. List of primers for lentiviral plasmid generation.

| Primer Name | Primer sequence |
|---------------------|---|
| LCv2-GFP.Gib.F | GATTACAAAGACGATGACGATAAGGGATCCGGTGAGGGCAGAGGAAGTC |
| LCv2-GFP.Gib. | ACAGTCGAGGCTGATCAGCGGGTTTAAACCTACTACTGCTAGAGATTTTCCACAC |
| LCv2-GFP.seq.L | ACCGGCCTGTACGAGACACG |
| LCv2-GFP.seq.R | GAAAGGACAGTGGGAGTGGCACC |
| VMD2.LCv2.GFP.Gib.F | GTGGCACCGAGTCGGTGCTTTTTTTGAATTCCAATTCTGTCATTTACTAGGGTGATGAAATTC |
| VMD2.LCv2.GFP.Gib.R | TGTACTTCTTGTCATGGTGGCAGCGCTCTATCGGCCGCGGGTACA |
| VMD2.LCv2.GFP.seq.L | GAATGAATACCGGGCTGCAGTCAAC |
| VMD2.LCv2.GFP.seq.R | GTCGGTGATCACGGCCCAG |

900
901

902 **Table S5. List of sgRNAs.**

903

904 Off-target (Doench et al, Nat Biotechnol., 2016) and on-target (Hsu et al, Nat. Biotechnol., 2013) scores

905 are also presented. Scores range from 0-100 with higher scores being better for both scoring systems.

906 Highest ranked off-target cut sites for each sgRNA are available in **Supplemental Data File D.**

907

| sgRNA Name | Sequence 5' - 3' | PAM | Chr | Position | Strand | Off-Target Score | On-Target Score |
|-------------------|-------------------------|------------|------------|-----------------|---------------|-------------------------|------------------------|
| A146K | CTTTGGTGCTGACGCTGCGC | AGG | 11 | 61955893 | -1 | 81.2 | 51.6 |
| R218C | GTGTCCCACTGAGTACACA | AGG | 11 | 61957403 | -1 | 56.3 | 67.2 |
| WT | GTGTCCCACTGAGTACGCA | AGG | 11 | 61957403 | -1 | 86.5 | 63.7 |
| N296H | CATCATCCTCTCCAAAGGGG | TGG | 11 | 61959521 | -1 | 54.0 | 64.6 |
| <i>AAVSI</i> | GGGGCCACTAGGGACAGGAT | TGG | 19 | 55115755 | +1 | 55.8 | 54.5 |

908

909

910 **Table S6. Lentivirus titers.**

911

| Lentivirus | Titer (Transduction units/ml) |
|--|--------------------------------------|
| <i>hVMD2-hBEST1-T2A-GFP</i> | 22x10 ⁶⁻⁷ |
| LCv2.R218C sgRNA | 81.91 x10 ⁶⁻⁷ |
| LCv2.WT sgRNA | 55.22 x10 ⁶⁻⁷ |
| LCv2. <i>AAVS1</i> sgRNA | 45.43 x10 ⁶⁻⁷ |
| <i>hVMD2-spCas9-T2A-GFP</i> LV R218C sgRNA | 74.16 x10 ⁶⁻⁷ |
| <i>hVMD2-spCas9-T2A-GFP</i> LV WT sgRNA | 71.16 x10 ⁶⁻⁷ |
| <i>hVMD2-spCas9-T2A-GFP</i> LV A146K sgRNA | 74.26 x10 ⁶⁻⁷ |
| <i>hVMD2-spCas9-T2A-GFP</i> LV N296H sgRNA | 68.91 x10 ⁶⁻⁷ |
| <i>hVMD2-spCas9-T2A-GFP</i> LV <i>AAVS1</i> sgRNA | 74.01 x10 ⁶⁻⁷ |

912

913

914 **Table S7. Primers for deep sequencing of DNA and cDNA.**

915

| Primer Name | Primer sequence |
|--------------------|----------------------------|
| MT.C.OT.5v2.HTS.F | GTTGGTTCCTGAAGATGGGCAG |
| MT.C.OT.5v2.HTS.R | CTGTCAAGGCCAAGTTCTGCTG |
| MT.C.OT.2.HTS.F | GCTAAATTCTGCTATAAAAGGAAGG |
| MT.C.OT.2.HTS.R | GCATTGCTTTAGAAAACCTCAGAAGT |
| MT.C.OT.3.HTS.F | AGTGAGACCAAGTTCTGACAGCA |
| MT.C.OT.3.HTS.R | GGCCTCTTCATACATACACATGCAC |
| MT.C.OT.4.HTS.F | CCTCCACATCTGCAGAAAAGTGT |
| MT.C.OT.4.HTS.R | GGCAGGGTTTGGTCTCCTACTT |
| MT.C.OT.5.HTS.F | GGATGGCTCTGGGTGGGTTT |
| MT.C.OT.5.HTS.R | CTTCCAACCTCTCCTCCCACCC |
| MT.C.OT.6.HTS.F | TGAGGTTCAGAATAGCTCAGCA |
| MT.C.OT.6.HTS.R | TGTTTCTGTGAAGCAAATCAAAGCT |
| MT.C.OT.7.HTS.F | TGTTTCTGTGAAGCAAATCAAAGCT |
| MT.C.OT.7.HTS.R | TGAGGTTCAGAATAGCTCAGCA |
| MT.C.OT.8.HTS.F | AAAGCATGGCGGGAGTGCTAA |
| MT.C.OT.8.HTS.R | TGACTAAATCCCTGGCATCGCT |
| MT.C.OT.9.HTS.F | GCCAGTAATTTTCCAAGGCTTCT |
| MT.C.OT.9.HTS.R | TTCTACTAGAACCTCCTTGAG |
| MT.C.OT.10.HTS.F | GTGACCTGACTTTGCTGAAAGGT |
| MT.C.OT.10.HTS.R | ACCTGAATTATCTCAAGCTCACT |
| AAVS1T2.HTS.F | ATGTGGCTCTGGTTCTGGGTAC |
| AAVS1T2.HTS.R | GAGACTAGGAAGGAGGAGGCCT |
| R218C.HTSv2.F | GTGTTTCAGAACCCCATCCCC |
| R218C.HTSv2.R | AGCCTAGTCCTCACCTGTGT |
| BEST.cDNA.HTSv2.F | GGTCGAATCCGGGACCCTATC |
| BEST.cDNA.HTSv2.R | GCCACAGTCACCACCTGTGTAT |
| AAVS1T2.HTS.F | ATGTGGCTCTGGTTCTGGGTAC |
| AAVS1T2.HTS.R | GAGACTAGGAAGGAGGAGGCCT |

916

917

918 **Table S8. Number of cells used for CaCC current density measurements.**
919

| Line | Replicate #1 | | Replicate #2 | | Total | |
|----------------------------|--------------|---------------------|--------------|---------------------|-----------|---------------------|
| | 0 calcium | 4.5 μ M calcium | 0 calcium | 4.5 μ M calcium | 0 calcium | 4.5 μ M calcium |
| Control | 3 | 3 | 5 | 3 | 8 | 6 |
| Isogenic control | 5 | 7 | 4 | 3 | 9 | 10 |
| R141H/A195V* | 4 | 3 | 4 | 5 | 12* | 12* |
| R141H/A195V +GA | 2 | 3 | 3 | 4 | 5 | 7 |
| R218C | 3 | 3 | 5 | 2 | 8 | 5 |
| R218C +GA | 6 | 7 | 3 | 4 | 9 | 11 |
| R218C +GE (R218C sgRNA) | 3 | 5 | 4 | 5 | 7 | 10 |
| N296H | 4 | 4 | 4 | 3 | 8 | 7 |
| N296H +GA | 4 | 3 | 2 | 4 | 6 | 7 |
| N296H +GE (N296H sgRNA) | 4 | 5 | 5 | 4 | 9 | 9 |
| A146K | 2 | 2 | 5 | 3 | 7 | 5 |
| A146K +GA | 4 | 2 | 4 | 3 | 8 | 5 |
| A146K +GE (A146K sgRNA) | 5 | 5 | 5 | 6 | 10 | 11 |
| A146K +GE (AAVSI sgRNA) | 4 | 3 | 5 | 3 | 9 | 6 |

920
921 *3 replicates were used for R141H/A195V. Replicate #3 for R141H/A195V had n=4 (0 calcium); n=4
922 (4.5 μ M calcium)
923

924 **References for Supplemental Tables**

925 Doench, J.G., Fusi, N., Sullender, M., Hedge, M., Vaimberg, E.W., Donovan, K.F., Smith, I., Tothova, Z., Wilen
926 C., Orchard, R., Virgin, H.W., Listgarten, J., and Root, D.E. (2016). Optimized sgRNA design to maximize
927 activity and minimize off-target effects of CRISPR-Cas9. *Nat Biotechnol* 34(2), 184-191.

928
929 Hsu, P.D., Scott, D.A., Weinstein, J.A., Ran, F.A., Konermann, S., Agarwala, V., Li, Y., Fine, E.J., Wu, X.,
930 Shalem, O., Cradick, T.J., Marraffini, L.A., Bao, G., and Zhang, F. (2013). DNA targeting specificity of RNA-
931 guided Cas9 nucleases. *Nat Biotech* 31, 827-832.

932

- 933 Sanjana, N., Shalem, O., and Zhang, F. (2014). Improved vectors and genome-wide libraries for CRISPR
934 screening. *Nat Methods* *11*, 783-784.
- 935
- 936 Singh, R., Shen, W., Kuai, D., Martin, J.M., Guo, X.R., Smith, M.A., Perez, E.T., Phillips, M.J., Simonett, J.M.,
937 Wallace, K.A., *et al.* (2013b). iPS cell modeling of Best disease: insights into the pathophysiology of an inherited
938 macular degeneration. *Hum Mol Genet* *22*, 593-607.
- 939
- 940 Steyer, B., Bu, Q., Cory, E., Jiang, K., Duong, S., Sinha, D., Steltzer, S., Gamm, D., Chang, Q., and Saha,
941 K. (2018). Scarless Genome Editing of Human Pluripotent Stem Cells via Transient Puromycin Selection.
942 *Stem Cell Reports* *10*, 642-654.